

Stabilization of active tissue deformation by a dynamic signaling gradient

Muhamed Ibrahimi^{1,2} and Matthias Merkel^{1,*}

¹*Aix Marseille Univ, Université de Toulon, CNRS, CPT (UMR 7332),
Turing Centre for Living Systems, Marseille, France.*

²*Laboratory of Artificial and Natural Evolution (LANE), Department of Genetics and Evolution,
University of Geneva, 1211 Geneva, Switzerland.*

(Dated: September 3, 2025)

A key process during animal morphogenesis is oriented tissue deformation, which is often driven by internally generated active stresses. Yet, such active oriented materials are prone to well-known instabilities, raising the question of how oriented tissue deformation can be robust during morphogenesis. Here we study under which conditions active oriented deformation can be stabilized by the concentration pattern of a signaling molecule, which is secreted by a localized source region, diffuses across the tissue, and degrades. Consistent with earlier results, we find that oriented tissue deformation is always unstable in the gradient-contractile case, i.e. when active stresses act to contract the tissue along the direction of the signaling gradient, and we now show that this is true even in the limit of large diffusion. However, active deformation can be stabilized in the gradient-extensile case, i.e. when active stresses act to extend the tissue along the direction of the signaling gradient. Specifically, we show that gradient-extensile systems can be stable when the tissue is already elongated in the direction of the gradient. We moreover point out the existence of a formerly unknown, additional instability of the tissue shape change. This instability results from the interplay of active tissue shear and signal diffusion, and it indicates that some additional feedback mechanism may be required to control the target tissue shape. Taken together, our theoretical results provide quantitative criteria for robust active tissue deformation, and explain the lack of gradient-contractile systems in the biological literature, suggesting that the active matter instability acts as an evolutionary selection criterion.

I. INTRODUCTION

Oriented tissue deformation is a key process during animal morphogenesis [1], including for instance body axis elongation [2–4] and organ formation [5–10]. In many cases, such tissue deformation is at least in part driven by internally generated active stresses [8, 10–13], and in recent years, deforming tissues have successfully been described as active materials [8, 14–21]. Moreover, to achieve persistent large-scale oriented deformation, tissues need some kind of tissue-wide orientational information, which can be represented for instance by a polar or a nematic field [8, 15, 19, 22, 23]. However, active polar or nematic materials are subject to the well-known Simha-Ramaswamy instability, where an initially globally ordered orientational field loses this order due to active flows [24–26]. This raises the question of how oriented tissue deformation can be stable during animal development.

In animals, oriented tissue deformation can be affected by tissue-scale concentration patterns of signaling molecules. Such patterns of signaling molecules are known to coordinate developmental processes on the tissue or even organism scale [1]. Signaling molecules can provide *positional* information, in which case they are called morphogens [3, 27–31]. Yet, in some cases, concentration gradients of signaling molecules also provide *orientational* information, which defines the axis of active

stresses driving oriented tissue deformation [5–7, 12, 32], typically by guiding cellular polarity and cell rearrangements [2, 4, 6, 12, 33]. Such alignment of orientational information with signaling gradients has recently also been discussed theoretically [34].

In a recent publication [35], we theoretically showed that oriented tissue deformation can be stabilized by signaling gradients. We used a hydrodynamic model for an active polar material, and showed that the gradient of a scalar signaling field can stabilize the otherwise unstable material. We showed that if the scalar field advects with the material flows [36, 37], the stability of oriented material deformation depends on the coupling between scalar field gradient direction and deformation axis. In the gradient-extensile case, i.e. when anisotropic active stresses act to extend the material along the gradient direction, the scalar field can stabilize the active material deformation. However, in the gradient-contractile case, i.e. when anisotropic active stresses act to contract the material along the gradient direction, the deformation is unstable. Yet, one could always stabilize even a gradient-contractile system by sufficiently increasing the diffusion of the signaling molecule.

In our past publication [35], we have created a uniform scalar field gradient in a simple way through appropriate boundary conditions. While providing advantages for analytical calculations, this is quite different from the real mechanism creating signaling gradients in developing biological tissues [1, 28, 29, 38–40]. Signaling molecules are typically produced by some source region, diffuse across the tissue, and degrade [40, 41]. As a consequence, depending on the source region, this can lead to approxi-

* matthias.merkel@cnrs.fr

mately exponentially decaying [38, 39, 42, 43] or periodic [44, 45] concentration profiles. However, it is not known how such signaling molecule dynamics would affect stability of active oriented tissue deformation.

In this article, we study the stability of active tissue deformation when accounting for more realistic signaling dynamics (Figure 1A). We consider an active viscous tissue with local flow velocity $\mathbf{v}(\mathbf{r}, t)$, where active stresses are defined by the gradient of a signaling molecule concentration field $c(\mathbf{r}, t)$. The signaling field $c(\mathbf{r}, t)$ is in turn secreted by a source region that is defined by a field $s(\mathbf{r}, t)$, which is conserved and only advects with tissue flows. The signaling field $c(\mathbf{r}, t)$ not only advects with tissue flows, but also diffuses and degrades at constant rates everywhere.

Using linear stability analysis, we find that gradient-contractile tissues are always unstable, consistent with our earlier findings [35]. Yet, we also show that for our more realistic signaling dynamics, a gradient-contractile system can never be stabilized by diffusion. We further show that gradient-extensile systems can be stable, in particular if the tissue is longer in the direction of the gradient than transversal to it. Finally, as soon as the system deforms, we find that an additional instability can appear for both gradient-extensile and gradient-contractile cases, arising from the interaction between shear and diffusion. This instability may point to the necessity of an additional control mechanism for the final tissue dimensions.

In the following, we first introduce the model in section II. We then study the case of a uniform gradient in both $s(\mathbf{r}, t)$ and $c(\mathbf{r}, t)$ for fixed system size in section III, for which the linear stability can be computed analytically. Next, in section IV, still for fixed system size, we study the more realistic case of a localized source $s(\mathbf{r}, t)$, which gives rise to a non-uniform signaling gradient $c(\mathbf{r}, t)$. We then discuss the stability of freely deforming systems in section V. Finally, in section VI, we discuss our findings in the context of the biological literature.

II. MODEL

A. Hydrodynamic fields and bulk dynamics

We describe the tissue as a 2D active material, where we consider three interacting hydrodynamic fields: a scalar field $s(\mathbf{r}, t)$, which describes the source, i.e. cells in the tissue which secrete the signaling molecule; a scalar field $c(\mathbf{r}, t)$, which describes the signaling molecule concentration; and a vector field $\mathbf{v}(\mathbf{r}, t)$, which describes the tissue flows (Figure 1A). We find that literature values for the respective rates of tissue deformation \tilde{v}_{xx}^0 , signaling molecule diffusion D/L^2 , where D is the diffusion coefficient and L denotes the linear dimension of the tissue, and signaling molecule degradation k_d are of roughly similar orders of magnitude (Figure 1B), suggesting that none of them can be easily neglected, and we thus include

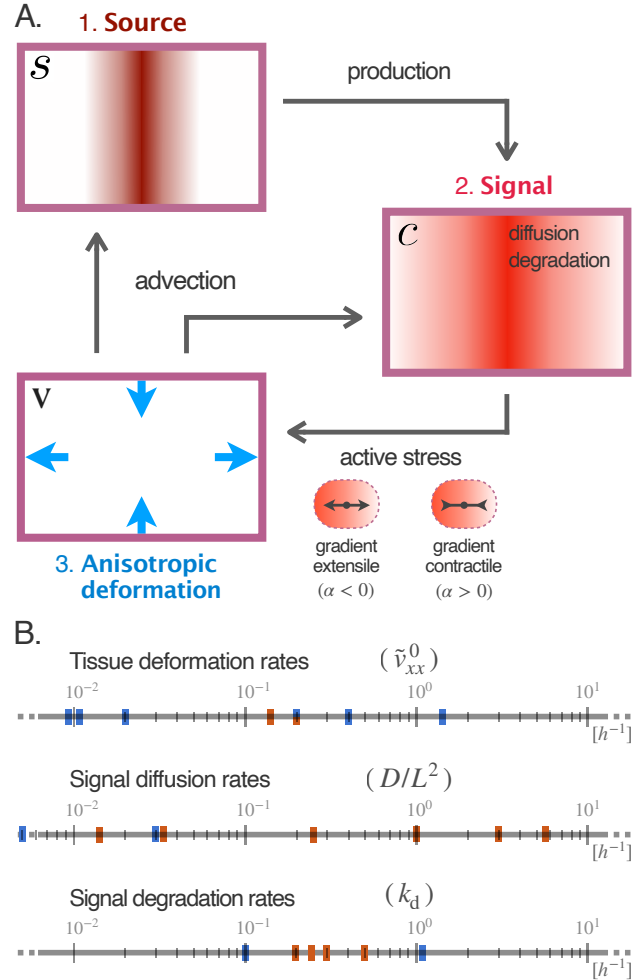


FIG. 1. (A) Hydrodynamic model. A spatially varying source field $s(\mathbf{r}, t)$ secretes a signaling molecule with concentration $c(\mathbf{r}, t)$, which also diffuses and degrades. The gradient of c creates extensile/contractile active anisotropic stresses, which drive viscous flows with velocity $\mathbf{v}(\mathbf{r}, t)$. These flows affect both source and signaling fields through advection. (B) Typical orders of magnitude for tissue deformation rates \tilde{v}_{xx}^0 (top), signal diffusion rates D/L^2 , where D is the diffusion coefficient and L is the linear dimension of the corresponding tissue (middle), and signal degradation rates k_d (bottom) from the biological literature. Blue marks are data from the fruit fly *Drosophila melanogaster*, and orange marks are data from zebrafish, *Danio rerio*. Tissue deformation rates in the fruit fly were estimated from image time series of: egg chamber [46, 47], dorsal thorax [12], pupal wing [8], hindgut [5, 48], renal tubules [7], and germ-band [11]; and in zebrafish from mesodermal explants [49] and the tailbud [50]. Signaling molecules: Decapentaplegic in the fruit fly [38, 40, 51]; Cyclops, Squint, Lefty1 and Lefty2 in zebrafish [29, 42].

all three effects in our model.

The source field $s(\mathbf{r}, t)$, which describes signaling molecule secretion, only advects with material flows:

$$\frac{\partial s}{\partial t} + \partial_i(v_i s) = 0, \quad (1)$$

where ∂_i denotes the partial derivative with respect to the spatial coordinate $r_i \in \{x, y\}$. Here and in the following, we label spatial dimensions by Latin indices i, j, \dots and adopt the Einstein notation of summing over repeated indices.

The signaling field $c(\mathbf{r}, t)$ follows a generalized conservation equation:

$$\frac{\partial c}{\partial t} + \partial_i(v_i c) = k_p s - k_d c + D \partial_i^2 c. \quad (2)$$

Here, we have introduced production rate k_p , degradation rate k_d , and diffusion coefficient D . Note that there are several intra- and extra-cellular mechanisms of signaling molecule transport [29] – here we describe the emergent *effective* transport on large length scales by advection and diffusion.

Tissue flows $\mathbf{v}(\mathbf{r}, t)$ are governed by overdamped, incompressible, viscous dynamics:

$$\partial_i \sigma_{ij} = 0, \quad (3)$$

$$\partial_i v_i = 0, \quad (4)$$

where the stress tensor is given by

$$\sigma_{ij} = 2\eta \tilde{v}_{ij} - \Pi \delta_{ij} + \tilde{\sigma}_{ij}^a. \quad (5)$$

Here, η is the shear viscosity, $\tilde{v}_{ij} := (\partial_i v_j + \partial_j v_i - \partial_k v_k \delta_{ij})/2$ is the shear rate tensor, Π is the hydrostatic pressure, and we use the following expression for the active stress $\tilde{\sigma}_{ij}^a$:

$$\tilde{\sigma}_{ij}^a = \alpha \left[(\partial_i c)(\partial_j c) - \frac{1}{2}(\partial_k c)^2 \delta_{ij} \right]. \quad (6)$$

This expression for the active anisotropic stress is the same as in Active Model H [52, 53]. Its direction is determined by the sign of the coefficient α : For $\alpha < 0$, the activity is gradient-extensile, i.e. it acts to extend the material along the local c gradient direction and contract perpendicularly; while for $\alpha > 0$, the activity is gradient-contractile, i.e. it acts to contract the material along the c gradient direction and extend perpendicularly (Figure 1A).

The expression for the active stress, Eq. (6), is motivated by what is known about developing biological tissues. Specifically, anisotropic internal stresses are usually generated by an anisotropic distribution of cytoskeletal elements within cells. Such an anisotropic distribution is created by cell polarity, which in turn can be controlled by signaling gradients [7, 12, 33, 54, 55]. Rather than explicitly including cell polarity as polar field [35], we assume here for simplicity a direct coupling of active stresses to the signaling gradient. This corresponds to the limit where the time scales involved in couplings active stresses to the signaling gradient are fast as compared to the other time scales of the system. While this is clearly a simplification, we do not expect the fundamental results of the analysis do not differ much in this limit, as suggested by our earlier work [35]. Note that Eq. (6) represents the lowest-order term for a coupling of an active, anisotropic stress to a scalar field [52].

B. Boundary Conditions

We use periodic boundary conditions, where the periodic box has generally time-dependent dimensions $L_x(t) \times L_y(t)$ and constant area, $L_x(t)L_y(t) = \text{const}$. Throughout this article, we always use one of the following two boundary conditions:

1. We fix the system dimensions L_x and L_y , or
2. we allow the system to freely deform by fixing the externally applied stress to zero, which results in a pure shear deformation of the periodic box. Integration of Eq. (5) implies that the instantaneous box shear rate is

$$\frac{1}{L_x} \frac{dL_x}{dt} = -\frac{\alpha}{4\eta L_x L_y} \int [(\partial_x c)^2 - (\partial_y c)^2] dA, \quad (7)$$

where the integral is over the whole periodic box.

We apply fixed system dimensions in section III and section IV, and study a freely deforming system in section V.

We investigate the stability of two stationary states: (i) a state where a linear source profile s gives rise to a linear signaling profile c , and (ii) a state where a localized source s generates a spatially decaying signaling field c . In both cases, the amplitude of the source field is defined by a constant s_b . In case (i), which we study in section III, the boundary conditions are periodic with the exception of the vertical boundaries for the scalar fields s and c , where we set for all $y \in [0, L_y]$:

$$s(0, y) = s(L_x, y) - s_b, \quad (8)$$

$$c(0, y) = c(L_x, y) - \frac{k_p}{k_d} s_b, \quad (9)$$

with fixed s_b . These modified conditions remove the discontinuity that would otherwise appear for linear profiles in s and c at the boundary, and thus ensure that linear s and c profiles can be stationary [35]. In case (ii), which we study in section IV and section V, we use standard periodic boundary conditions without offset.

C. Dimensionless equations

We nondimensionalize the set of equations Eqs. (1)–(9) in the following way:

- We choose the unit of length such that the system area is one, $L_x L_y = 1$.
- We choose the unit of the signaling field c such that $k_p = k_d$.
- We choose the units of time and of the source field s , such that the free deformation rate of a squared system is 1. To this end, we set $|\alpha|/4\eta = 1$, and in case (i) of a linear gradient, we also set $s_b = 1$, while in case (ii) of a non-uniform gradient, we fix s_b as described in section IV (Appendix E1).

The last condition allows to compare the linear stability of systems with different source profiles, because the reference time scale is always the respective free deformation rate.

Rescaled accordingly, the dimensionless equations read:

$$\frac{\partial s}{\partial t} + v_i \partial_i s = 0, \quad (10)$$

$$\frac{\partial c}{\partial t} + v_i \partial_i c = (D \partial_i^2 - k_d) c + k_d s, \quad (11)$$

$$0 = \frac{1}{4} \partial_i^2 v_j - \partial_j \Pi' + \text{sgn}(\alpha) \partial_i [(\partial_i c)(\partial_j c)], \quad (12)$$

$$\partial_i v_i = 0. \quad (13)$$

Here, we have introduced the sign function, $\text{sgn}(\alpha) := \alpha/|\alpha|$, and have set $\Pi' := \Pi + \text{sgn}(\alpha)(\partial_k c)^2/2$. The offset introduced at the boundary conditions in Eqs. (8) and (9) is rescaled to 1 for both scalar fields.

III. LINEAR SOURCE PROFILE

To build intuition, we study for fixed box dimensions $L_x = L_y = 1$ the linear stability of a stationary state with linear spatial profiles in s and c (Figure 2A), given by:

$$s_0 = x, \quad c_0 = x, \quad \mathbf{v}_0 = \mathbf{0}. \quad (14)$$

There are no flows in the stationary state, because the gradient of c is homogeneous, and thus the active stress is homogeneous across the system of fixed dimensions.

In this case, linear stability can be computed analytically. When we add a small perturbation around this state,

$$s = x + \delta s, \quad c = x + \delta c, \quad \mathbf{v} = \delta \mathbf{v}, \quad (15)$$

and linearize the dynamics, only constant prefactors occur. As a consequence the solutions in $(\delta s, \delta c, \delta \mathbf{v})$ are spatial Fourier modes with wave vectors $\mathbf{q} = q(\cos \phi, \sin \phi)$, whose amplitudes grow or shrink exponentially with time t (Appendix D).

We first discuss the limit without diffusion, $D = 0$. When we subtract the linearized versions (Appendix C) of source and signaling dynamics, Eqs. (10) and (11), we obtain:

$$\frac{\partial}{\partial t} (\delta c - \delta s) = -k_d (\delta c - \delta s). \quad (16)$$

Thus, any difference between signaling field c and source field s decays at rate k_d . In addition, the combination of signaling dynamics and generated active flows, Eqs. (11)–(13), leads to the same results as for a single scalar field discussed in earlier publications [35, 53] (Appendix D 1). Specifically, for the combined perturbation field $\delta c_{\text{eff}} := \delta c + k_d/\omega_{\text{act}} \delta s$, we obtain (Eq. (D8) in Appendix D):

$$\frac{\partial \delta c_{\text{eff}}}{\partial t} = \omega_{\text{act}} \delta c_{\text{eff}}, \quad (17)$$

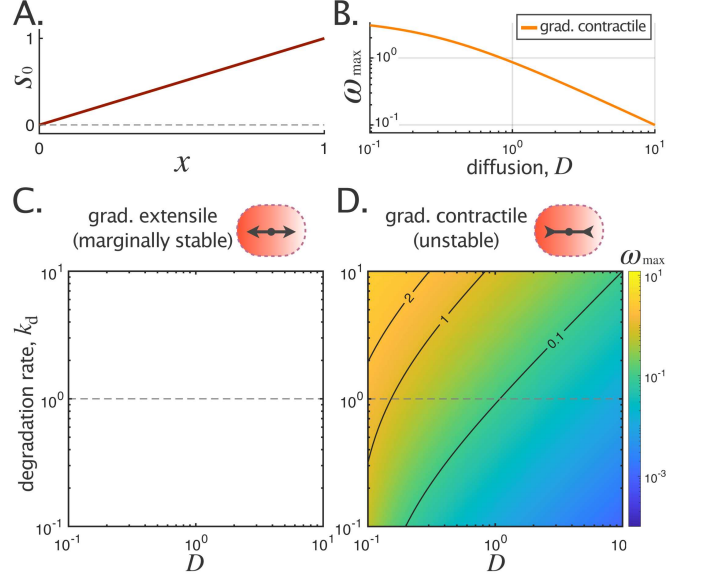


FIG. 2. Stability of a fixed-size system with a linear source profile: gradient-extensile systems are marginally stable, whereas gradient-contractile systems are unstable. (A) The linear source profile, $s_0(x) = x$ in dimensionless units. In the stationary state, $c_0(x) = s_0(x)$. (B) Effect of signaling molecule diffusion D on the maximal perturbation growth rates ω_{max} of a gradient-contractile system (with $k_d = 1$), plotted in log-log scaling. (C,D) Maximal perturbation growth rates in the $D-k_d$ parameter space show that gradient-extensile systems (C) are marginally stable and that gradient-contractile systems (D) are always unstable.

where $\omega_{\text{act}} := 4 \text{sgn}(\alpha) \sin^2 \phi$ is the perturbation growth rate created by the active flows. It takes the same form without source field [35]. Thus, without diffusion, the system is marginally stable in the gradient-extensile case, i.e. the maximal perturbation growth rate is zero, and unstable in the gradient-contractile case.

In the presence of diffusion, $D > 0$, gradient-extensile systems remain marginally stable (Figure 2C). However, gradient-contractile systems can *not* be stabilized by diffusion, even though the maximal perturbation growth rate decreases with diffusion (Figure 2B,D). This is in contrast to earlier findings for a system with a boundary-imposed signaling gradient, where we found that diffusion *can* stabilize gradient-contractile systems [35]. To understand where the difference comes from, we consider the limit of very large D . The linearized version of the signaling dynamics, Eq. (11), in Fourier space reads:

$$\frac{\partial \delta c}{\partial t} + \delta v_x = -(D q^2 + k_d) \delta c + k_d \delta s. \quad (18)$$

The flow field $\delta \mathbf{v}$ enters on the left-hand side due to advection, where $\partial_x c_0 = 1$ in dimensionless units. The flow $\delta \mathbf{v}$ is actively created by the signaling field itself through Eqs. (12) and (13), and its x component in Fourier space reads: $\delta v_x = -\omega_{\text{act}} \delta c$, with the active flow time scale ω_{act} introduced before. Denoting the minimal non-zero

wave vector magnitude in our system by q_{\min} , we take the limit where Dq_{\min}^2 is much larger than all other relevant time scales in the system. In this case, according to Eq. (18), the Fourier amplitude δc for each wave vector relaxes adiabatically fast towards

$$\delta c \simeq \frac{k_d}{Dq^2} \delta s. \quad (19)$$

This effectively corresponds to a system where we again just have a single scalar field s , which advects with active tissue flows \mathbf{v} , but does *not* diffuse. The active tissue flows are generated by the perturbations of c , and their x component is given by $\delta v_x = -\omega_{\text{act}} \delta c \simeq -(\omega_{\text{act}} k_d / Dq^2) \delta s$. Inserting this into the linearized version of the source dynamics in Fourier space, we obtain (compare to Eq. (17)):

$$\frac{\partial \delta s}{\partial t} = -\delta v_x = \frac{\omega_{\text{act}} k_d}{Dq^2} \delta s. \quad (20)$$

Thus, the perturbation growth rate is given by the growth rate without diffusion, ω_{act} , multiplied by k_d / Dq^2 (Figure 2B). As a consequence, gradient-contractile systems are unstable even in the limit of a large diffusion constant. The reason for this is that the source field itself advects with the active flows, but does not diffuse. For the same reason, gradient-extensile systems remain only marginally stable even in the presence of signaling molecule diffusion.

IV. LOCALIZED SOURCE PROFILE

We next discuss how the linear stability changes when the source profile is not linear but is instead localized to some region of finite width w . This is motivated by what we know about developing biological tissues [1, 38, 41, 45]. In this section, we discuss a fixed-size system $L_x = L_y = 1$, while in the next one (section V) we discuss a freely deforming system.

As initial state, we use a source profile defined by a *von Mises* distribution, which is a generalization of a Gaussian to periodic boundary conditions:

$$s_0(\mathbf{r}) = s_b \left[\exp \left(\frac{\cos(q_0 x)}{(q_0 w)^2} \right) - \exp \left(-\frac{1}{(q_0 w)^2} \right) \right] \quad (21)$$

with $q_0 := 2\pi/L_x$. Here, w is a parameter that adjusts the width of the source region, the second term in Eq. (21) ensures that $s_0(\mathbf{r})$ is zero at its minimum, and s_b is a prefactor whose value is fixed such that the box deformation rate is normalized to one (Eq. (E1) in Appendix E1). As initial signaling field, we choose the c field that is stationary in the absence of flows for the source given by Eq. (21). In Fourier space:

$$c_0(\mathbf{q}) = \frac{k_d}{k_d + Dq^2} s_0(\mathbf{q}). \quad (22)$$

Thus, for $D = 0$, signaling and source profiles coincide, and examples for $s_0(x) = c_0(x)$ for different w values are shown in Figure 3A. Meanwhile, finite diffusion $D > 0$ smoothens the signaling profile $c_0(x)$ as compared to the source profile $s_0(x)$ (Figure 3B).

In this initial state, there are no flows in the system, $\mathbf{v}_0 = \mathbf{0}$. This is because the active stress in this case is parallel to the x axis and homogeneous along the y axis, because of incompressibility, and because of the fixed system size, which together imply that there are no Stokes flows (Appendix B 2).

Numerical simulations of the full dynamics, Eqs. (10)–(13), are shown in Figure 3C,D and in Movies S1, S2 (shown is the source field). We find that with chosen parameters ($w = 1/2\pi$, $k_d = 1$, and $D = 10^{-2}$), the gradient-extensile system appears to be stable until simulation time $t = 3$ (Figure 3C), yet an instability becomes apparent at much later times (Figure 5A in Appendix E and Movie S1). Meanwhile, the gradient-contractile system shown an instability already early on (Figure 3D and Movie S2).

For a more systematic characterization of the system's stability, we perform again a linear stability analysis. While the eigenmodes of the linearized dynamics still grow or shrink exponentially with time, they can only be represented by a superposition of several spatial Fourier modes (Appendix C 2). We thus compute the perturbation eigenmodes and their respective growth rates numerically (Appendix C 3). Note that due to the numerical Fourier-space convolutions, we also find aliasing effect arising from a finite spatial discretization, which we treat using standard methods in the field (Appendix C 3).

We find again that gradient-contractile systems are always linearly unstable (Figure 3E,F,H,J). Specifically, systems are more unstable when the source width is below $w \lesssim 0.06L_x$ (Figure 3F,H). Moreover, increasing the diffusion coefficient D decreases the perturbation growth rate, but it never reaches zero. Instead, in contrast to the linear gradient (section III), the maximum growth rate converges to a finite constant in the limit of large diffusion, $D \rightarrow \infty$ (Figure 6, Appendix E 2). It converges to a finite constant, because we non-dimensionalize rates with respect to the free deformation rate, which also decreases as diffusion D becomes larger due to an increased smoothing of c (Appendix E 2). This is different from the linear-gradient scenario (section III), where a constant signaling gradient, and thus a constant free deformation rate is imposed by the boundary conditions.

For gradient-extensile systems, the situation is more complex than for a linear gradient. Specifically, we find that the stability depends on the aspect ratio of the system. For aspect ratios L_x/L_y below 2...3, the system can be unstable, while it is numerically marginally stable for aspect ratios above (Figure 3E,G). Here, by “numerically marginally stable” we mean that we numerically cannot distinguish between marginally stable and numerically small, but finite growth rates – indeed, this distinction is also irrelevant in practice for a real biological sys-

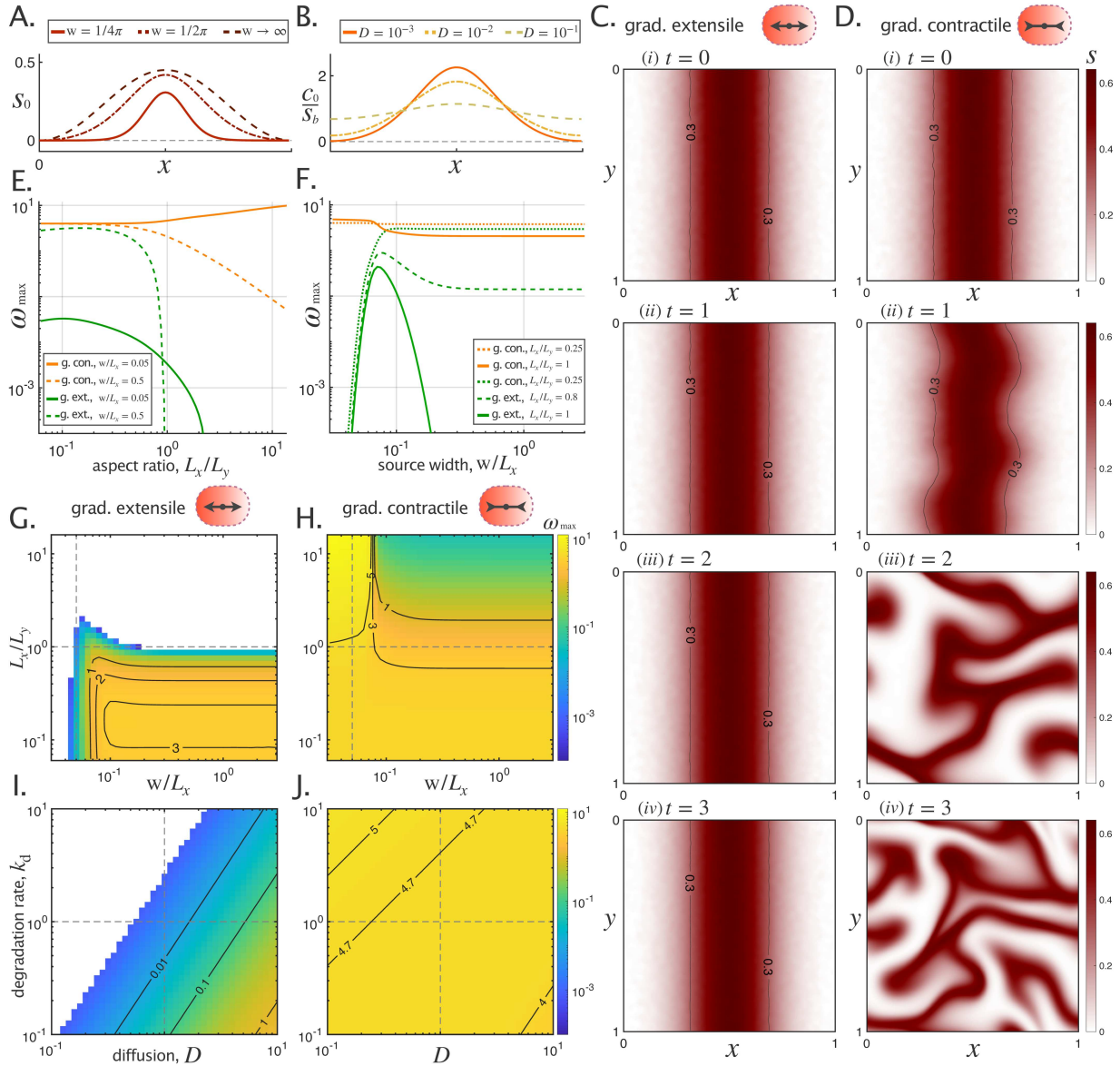


FIG. 3. Stability of a fixed-size system with a localized source profile. (A) The localized source profile $s_0(x)$ from Eq. (21) for different values of the source width w . (B) The localized signaling profile for different values of diffusion D . Here, $w = 1/2\pi$ in all cases. (C,D) Snapshots of the source profile from numerical simulations of the perturbed stationary state (with $w = 1/2\pi, D = 10^{-2}, k_d = 1$). While the source profile appears to be maintained in the (C) gradient-extensile case, it gets distorted in the (D) gradient-contractile case. (E) Effect of aspect ratio L_x/L_y on maximal perturbation growth rates ω_{\max} for different source widths. Gradient-contractile systems (orange) are always unstable, while gradient-extensile systems (green) have in some regions an ω_{\max} that can numerically not be distinguished from zero. Parameter values: $k_d = 1$ and $D = 1$. (F) Effect of the source width w/L_x on maximal perturbation growth rate for different box aspect ratios. Parameter values: $k_d = 1$ and $D = 1$. (G,H) Color plots of maximal perturbation growth rates for gradient-extensile (G) and gradient-contractile (H) couplings with varying source widths (horizontal axis) and aspect ratios (vertical axis). Solid black curves represent contours, whereas dashed gray lines corresponds to solid curves in panels E,F. Parameter values: $k_d = 1$ and $D = 1$. (I,J) Maximal perturbation growth rates in the $D-k_d$ parameter space for gradient-extensile (I) and gradient-contractile (J) couplings. Parameter values: $L_x/L_y = 1$ and $w/L_x = 0.05$.

tem. For aspect ratios, between ≈ 1 and $2 \dots 3$, the system is effectively unstable at intermediate source widths w/L_x between 0.04 and 0.2 and otherwise numerically marginally stable (white regions in Figure 3G). For even lower aspect ratios, we only observe numerical marginal

stability for very narrow sources with $w/L_x \lesssim 0.04$ (Figure 3F,G). The type of perturbation creating the most unstable mode appears to be always qualitatively the same: the local width of source and signaling is modulated by the flows created by the signaling perturbation

(Figure 5B). Finally, for given aspect ratio and source width, the system is generally more stable for small signaling length scales $\sqrt{D/k_d}$ (Figure 3I). In the large-diffusion limit, the maximum perturbation growth rate converges to a constant for the same reason as in the gradient-contractile case (Figure 6, Appendix E 2).

Note that even if gradient-extensile systems are formally unstable in a substantial part of the parameter space, for aspect ratios close to one the maximal perturbation growth rates can be several orders of magnitude smaller as compared to the gradient-contractile case. For instance, the maximal growth rate for the example simulation in Figure 3C, Figure 5A, and Movie S1 is positive, but very small, $\omega_{\max} = 1.9 \times 10^{-3}$ (as compared to $\omega_{\max} = 4.2$ in the gradient-contractile example in Figure 3D).

Taken together, the system is stable when it is more elongated in the direction of the gradient, or when the signaling length scale $\sqrt{D/k_d}$ is small.

V. FREELY DEFORMING SYSTEM

Here we study the linear stability of a system with a localized source s_0 , Eq. (21), under free deformation of the periodic box.

Even for homogeneous shear deformation, the source profile s_0 is not stationary, but becomes distorted due to advection with the box deformation (Figure 4A). To address this, following our earlier work [35], we define the co-deforming coordinates, $\bar{r} = (\bar{x}, \bar{y})$, based on the lab-frame coordinates $r = (x, y)$ by rescaling both axes:

$$\bar{x} := \frac{L_x(0)}{L_x(t)} x = l_x^{-1}(t)x \quad (23)$$

$$\bar{y} := \frac{L_y(0)}{L_y(t)} y = l_y(t)y, \quad (24)$$

where $l_x(t) := L_x(t)/L_x(0)$ is the box shear. Moreover, we also introduce a flow field in co-deforming coordinates, $\bar{v}(\bar{r})$, which corresponds to non-affine flows that may occur in addition to the pure shear deformation of the periodic box (Appendix A 3). Thus, for $\bar{v} = \mathbf{0}$ the system deforms affinely, and the source field $s_0(\bar{r})$ is stationary with respect to the co-deforming coordinates (Figure 4B).

Yet, in the general case of a finite diffusion constant, the signaling field c does not reach a stationary state – not even in co-deforming coordinates. This is because diffusion as observed in co-deforming coordinates depends on box shear l_x through the transformation rules in Eqs. (23) and (24). Thus, as a consequence of the permanently changing l_x , there is no stationary state in the freely deforming case. Hence, no standard linear stability analysis is possible – we instead analyze the local Lyapunov exponents of the system.

To compute the local Lyapunov exponents, we consider the system state combining source and signaling profiles in co-deforming coordinates with box shear,

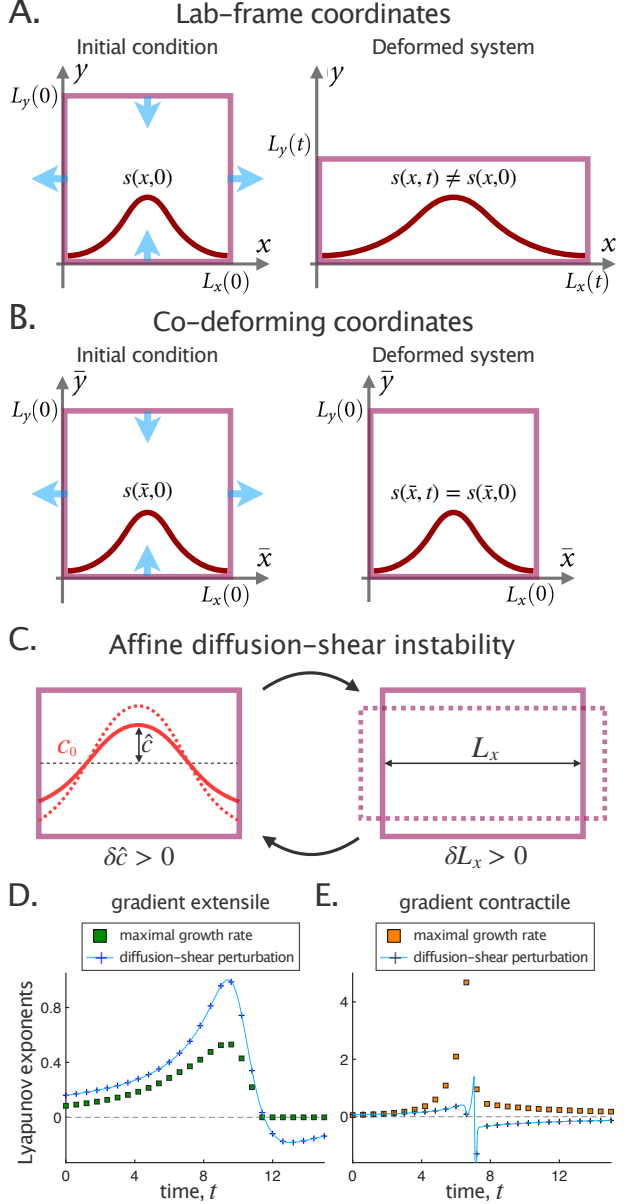


FIG. 4. Stability of a freely deforming system with a diffusive signaling molecule, studied in co-deforming coordinates. (A) In lab-frame coordinates, a localized source $s(r, t)$ is not stationary when the system deforms affinely, since its width changes proportionally with the system dimension L_x due to advection. (B) However, in co-deforming coordinates, Eqs. (23) and (24), the localized source $s(\bar{r}, t)$ remains stationary under affine deformation. (C) Illustration of the affine diffusion-shear instability: diffusion reduces the amplitude \hat{c} of the signaling field, but a larger L_x decreases the effective diffusion coefficient observed in co-deforming coordinates. Thus, a larger L_x leads to a larger \hat{c} , which in turn increases active shear and thus L_x . (D) Local Lyapunov exponents (LLE) for the gradient-extensile system over time. Green crosses indicate the numerically computed LLE of the affine diffusion-shear perturbation with the largest growth rate, and the blue curve displays the analytical prediction according to Eq. (F9) in Appendix F 2a. Green squares denote the maximal LLE of all other perturbations. (E) The same results as in panel D, but for the gradient-contractile system.

$\vec{z}(t) = [s(\vec{r}, t), c(\vec{r}, t), l_x(t)]$. This state constantly evolves through Eqs. (7) and (10)–(13), which we summarize here as $d\vec{z}/dt = \vec{F}(\vec{z})$. As initial condition, we use the source profile s_0 from Eq. (21), and the corresponding signaling profile c_0 that *would* be stationary in a fixed system, Eq. (22). To simplify our discussion here, we will focus on the limit $w \rightarrow \infty$, where the source $s_0(\mathbf{r})$ given by Eq. (21) corresponds to a cosine profile, $s_0(\mathbf{r}) \sim \cos(2\pi x/L_x) + 1$. The corresponding signaling profile is then also a cosine profile. We discuss the unperturbed box dimension dynamics, $l_x(t)$, in Appendix F 1, and here focus only on the perturbation dynamics.

Local Lyapunov exponents characterize whether and how quickly two slightly different solutions, \vec{z} and \vec{z}' , converge or diverge. The difference between both, $\delta\vec{z} := \vec{z}' - \vec{z}$, follows the dynamics $d\delta\vec{z}/dt = J(\vec{z}) \cdot \delta\vec{z}$, where $J(\vec{z})$ is the Jacobian of $\vec{F}(\vec{z})$. The local Lyapunov exponents at \vec{z} are then given by the eigenvalue spectrum of $J(\vec{z})$. When applied to a stationary state, this approach coincides with linear stability analysis.

In the limit of no diffusion, $D = 0$ (previous section, section IV), the linearized dynamics of source and signaling, Eqs. (C4) and (C5) (Appendix C 1), do not depend on the perturbation of the box shear, δl_x . Thus, the perturbation dynamics of s and c decouples from that of l_x , and most of the Lyapunov spectrum corresponds to the eigenvalue spectrum of the fixed system (section IV). The remaining eigenvalue of the local Lyapunov spectrum is given by the system size perturbation dynamics:

$$\frac{d\delta l_x}{dt} = \frac{\text{sgn}(\alpha)}{l_x^2(t)L_x^2(0)} \delta l_x. \quad (25)$$

The prefactor in this equation is positive for gradient-contractile systems and negative for gradient-extensile systems. Hence, for $D = 0$, the gradient-contractile system has positive local Lyapunov exponents, i.e. the system dynamics strongly depends on the initial conditions. Meanwhile, for gradient-extensive systems, the maximal local Lyapunov exponent is given by the maximal eigenvalue for the fixed-size system (section IV).

For finite diffusion, $D > 0$, the equations defining the linearized dynamics, Eqs. (C4)–(C6), are all coupled to each other and the full Jacobian needs to be diagonalized in order to obtain the local Lyapunov exponents. At each time point of the trajectory $\vec{z}(t)$, we plot the maximal Lyapunov exponent in Figure 4D,E.

We first discuss the gradient-extensile case, where we find here that the maximal perturbation growth rate can be positive (blue crosses in Figure 4D). However, at later times, when l_x becomes larger (green curves in Figure 7B, section F 1), the maximal growth rate becomes zero (green squares in Figure 4D). This fastest growing perturbation mode (blue crosses in Figure 4D), which we call here “affine diffusion-shear perturbation”, is different from the active scalar matter instability [35, 53]. Specifically, it does not affect the non-affine part of the flow field, \vec{v} or the source field s . Moreover, the signaling profile keeps its cosine shape, and only its amplitude \hat{c}

and the box shear l_x are affected by the perturbation. The positive growth rate of this mode arises from the fact that diffusion diminishes the amplitude of the signaling cosine profile, \hat{c} . Thus, increasing l_x by some positive amount δl_x decreases the effect of diffusion, which acts to increase \hat{c} and thus the integrated squared signaling gradient, which in turn acts to further increase l_x (Figure 4C). In Appendix F 2a, Eq. (F9), we obtain an analytical prediction for its growth rate (light blue curve in Figure 4D), which matches our numerical results (blue crosses). From our analytical prediction, we find that this instability appears as long as the diffusion length $\lambda := \sqrt{D/k_d}$ is larger than L_x , or more precisely $\lambda > L_x/2\pi\sqrt{3}$ (Appendix F 2a). Remarkably, for large diffusion, this instability does not disappear even when introducing an arbitrary non-linearity into the active stress (Appendix G).

For the gradient-contractile case, we find several modes with a positive growth rate (orange squares in Figure 4E). Moreover, we again have an eigenmode of the Jacobian that is an affine diffusion-shear perturbation (crosses in Figure 4E, compare to the predicted growth rate marked by the light blue curve).

Finally, in Appendix F 2b we study the affine diffusion-shear instability for the general case of a *finite* source width w . We find a positive growth rate whenever the order of magnitude of the diffusion length becomes larger than the source width, $\lambda \gtrsim w$ (Appendix F 2b).

VI. DISCUSSION

In developing animals, biological tissues can undergo active anisotropic deformation [1]. However, classical active matter results predict that such deformations are unstable under certain conditions [24, 25, 53]. In several systems, the local direction of active tissue deformation is controlled by the gradient of a signaling molecule concentration field [7, 12, 33]. Such signaling molecules are typically produced by the cells in a localized source region of the tissue, and they can form gradients through diffusion and degrade [1]. However, both signaling pattern and source region are also advected by the flows generated by the active deformation [36]. Here, we study the stability of a system which includes source field, signaling field, and signaling-gradient-controlled active tissue deformation. We find that systems where the active stresses are gradient-contractile are always unstable, while gradient-extensile can be marginally stable under certain conditions. Our findings are consistent with, and potentially explain, an observed abundance of gradient-extensile systems in the biological literature [3, 5, 7, 32, 44, 47, 49, 54, 56, 57] and the virtual absence of gradient-contractile systems (also discussed in [58]), suggesting that the instability discussed here may act as an evolutionary selection criterion.

In our previous work, we studied a simplified signaling dynamics, where the overall gradient was imposed by

the boundary conditions [35]. Here, we show that more realistic signaling dynamics, including secretion, diffusion, and degradation, lead to a number of important differences. First, in the gradient-contractile case, neither degradation nor diffusion can stabilize the system. While diffusion can decrease the growth rates of perturbations, we find that it never suffices to fully stabilize the system. This is because both signal and source fields are advected with the active flows, while only the signal diffuses. In the case of a linear source profile, the maximal perturbation growth rate could become arbitrarily small for a sufficiently large diffusion coefficient. However, in the case of a localized source, the maximal perturbation growth rate converges to a finite constant in the limit of a large diffusion coefficient (Appendix E2).

Second, we show that for a localized source region, gradient-extensile systems can become unstable whenever the tissue is too short in the direction of the gradient as compared to the transversal direction. Conversely, we numerically obtain marginal stability whenever the tissue is more elongated in the direction of the gradient or when the signaling lengths scale, $\sqrt{D/k_d}$, is small. However, we also find that even in the unstable regime, the maximum growth rate of gradient-extensile systems are often orders of magnitude smaller than the free deformation rate, in particular for aspect ratios close to one (Figs. 3E-J). It is not impossible that during development, biological tissues transiently accept an instability with a small growth rate until entering a stable regime once they become more elongated.

Finally, in deforming systems, an “affine diffusion-shear instability” can appear. Different from the other instabilities discussed here, which are all related to the Simha-Ramaswamy instability, the affine diffusion-shear instability does not require non-affine tissue flows. Instead, it is only reflected in an interplay between the amplitude of the signaling molecule and the overall tissue shear rate. This instability appears in tissues with a localized source whose width is smaller than the signaling diffusion length $\sqrt{D/k_d}$. It occurs even when adding any non-linearity in the way active stress depends on the signaling gradient (Appendix G). In many developing tissues, the signaling profile has a larger extent than the source region [1, 5, 38], and our work suggests that this instability should occur. Although this instability does not perturb the *patterns* of source, signaling molecule, or flow, it perturbs their amplitude and, most importantly, leads to a lack of control of the final tissue dimensions. This points to an additional feedback mechanism not included in our model that may be required to control the final tissue shape.

Our study further motivates experiments, and a key question is whether there are at all any gradient-contractile biological systems. There are many systems where signaling gradients are known to be necessary for active anisotropic tissue deformation. However, in most systems, it is not yet known whether the signal controls the directionality or only the magnitude of the

active stresses. For instance, there are still open debates about what controls the directionality of active stresses in what is probably the best-studied anisotropic tissue deformation process, which is germ band extension (GBE) in the fruit fly *Drosophila melanogaster*. Recent work on GBE proposed that a dorso-ventral signaling gradient modulates the *magnitude* of junctional myosin, which plays the role of active stresses [59]. Yet, different mechanisms have been proposed for the control of the myosin anisotropy and its *directionality*. Classically, these include anterior-posterior-oriented gradients [13, 44], which would correspond to a gradient-extensile coupling. But more recently, a group has proposed that a dorso-ventrally aligned tissue tension could provide a global mechanical orienting signal [36, 59]. Thus, in many cases more experiments are needed to cleanly disentangle the signals that merely modulate the amplitude of active stresses from those that control their direction. For instance, to modify the direction of the signaling pattern while keeping a similar overall magnitude, one could combine null-mutants with a graded over-expression [33] or the external supply of a gradient, e.g. through signaling-molecule-soaked beads [1, 27]. We believe that systematically combining insights from active matter theory with experiments in this way will help decode the biological mechanisms underlying oriented tissue deformation and its robustness.

ACKNOWLEDGMENTS

We thank the Centre Interdisciplinaire de Nanoscience de Marseille (CINaM) for providing office space. The project leading to this publication has received funding from France 2030, the French Government program managed by the French National Research Agency (ANR-16-CONV-0001), and from the Excellence Initiative of Aix-Marseille University - A*MIDEX. This project was also supported by the grant RobustTissue attributed to M.M. by the French National Research Agency (ANR-22-CE30-0039).

Appendix A: Co-deforming coordinates

1. Definition

Following Ref. [35], we introduce the co-deforming coordinate system, $(\bar{r}, \bar{t}) = (\bar{x}, \bar{y}, \bar{t})$, to analytically solve the linearized dynamics of systems under pure shear deformation.

The co-deforming coordinates map to the lab coordinates $(r, t) = (x, y, t)$ in the following way:

$$r_i = s_{ij}(\bar{t})\bar{r}_j \quad (A1)$$

$$t = \bar{t} \quad (A2)$$

where $\mathbf{s}(\bar{t})$ is a time-dependent shear tensor, given by

$$\mathbf{s}(\bar{t}) = \begin{pmatrix} l_x(\bar{t}) & 0 \\ 0 & l_x^{-1}(\bar{t}) \end{pmatrix}. \quad (\text{A3})$$

Thus, while at some time t , lab coordinates range from $0 \leq x < L_x(t)$ and $0 \leq y < L_y(t)$, co-deforming coordinates map these affinely to the box dimensions at time zero, with $0 \leq \bar{x} < L_x(0)$ and $0 \leq \bar{y} < L_y(0)$.

Note that for fixed system dimensions, where $L_x(t) = L_x(0)$, and thus $l_x(t) = 1$, both, co-deforming and lab coordinates coincide, $\bar{\mathbf{r}} \equiv \mathbf{r}$.

2. Partial derivatives

As a direct consequence of Eqs. (A1) and (A2), partial derivatives of some quantity f transform as:

$$\bar{\partial}_j f := \frac{\partial f(\bar{\mathbf{r}}, \bar{t})}{\partial \bar{r}_j} = (\partial_i f) s_{ij} \quad (\text{A4})$$

$$\bar{\partial}_t f := \frac{\partial f(\bar{\mathbf{r}}, \bar{t})}{\partial \bar{t}} = \partial_t f + (\partial_i f) \dot{s}_{ij} \bar{r}_j, \quad (\text{A5})$$

where $\partial_i f := \partial f(\mathbf{r}, t)/\partial r_i$, $\partial_t f := \partial f(\mathbf{r}, t)/\partial t$, and $\dot{s}_{ij} := ds_{ij}/dt = ds_{ij}/d\bar{t}$. Thus, the partial time derivative in co-deforming coordinates, $\bar{\partial}_t f$, i.e. for fixed $\bar{\mathbf{r}}$, includes a term related to the box shear rate as compared to the partial time derivative with respect to lab coordinates.

3. Velocity and velocity gradient

To obtain the mapping for the velocity field, we consider a tracer particle that is perfectly advected with the flows. The velocity of that tracer particle corresponds to a total time derivative $\bar{v}_i = dr_i/dt$, for which we obtain by insertion of Eq. (A1):

$$v_i = \dot{s}_{ij} \bar{r}_j + s_{ij} \bar{v}_j, \quad (\text{A6})$$

where $\bar{v}_i := d\bar{r}_i/dt = d\bar{r}_i/d\bar{t}$ is the co-deforming velocity, with $\bar{r}(\bar{t})$ being the tracer trajectory in co-deforming coordinates.

The first term in Eq. (A6) corresponds to a motion due to the affine transformation according to box coordinates. Thus, \bar{v}_i can be interpreted as the non-affine component of the flow field. This can also be seen more explicitly by computing the velocity gradient from Eq. (A6):

$$\partial_i v_j = v_{ij}^0 + s_{li}^{-1} s_{jk} \bar{\partial}_l \bar{v}_k, \quad (\text{A7})$$

where $v_{ij}^0 := s_{ki}^{-1} \dot{s}_{jk}$ is the average box deformation rate tensor. For s_{ij} as defined in Eq. (A3), the box deformation rate tensor is:

$$v_{ij}^0 = \begin{pmatrix} \dot{l}_x/l_x & 0 \\ 0 & -\dot{l}_x/l_x \end{pmatrix} = \begin{pmatrix} \dot{L}_x/L_x & 0 \\ 0 & -\dot{L}_x/L_x \end{pmatrix}. \quad (\text{A8})$$

4. Total derivative

To obtain a transformation formula for the convective derivative, we consider again our tracer and the presence of some spatio-temporal field f . The convective derivative corresponds to the total derivative of the value of f that the tracer locally sees. Thus, we expect analogous expressions for the convective derivative in both lab and co-deforming systems, $\dot{f} := df/dt = df/d\bar{t}$. Indeed, using Eqs. (A4), (A5), and (A6), we obtain:

$$\dot{f} = \partial_t f + v_i (\partial_i f) = \bar{\partial}_t f + \bar{v}_i (\bar{\partial}_i f). \quad (\text{A9})$$

5. Fourier transform

Moreover, we define the co-deforming Fourier transformation of a quantity f such that

$$f(\bar{\mathbf{r}}) = \sum_{\bar{\mathbf{q}}} f(\bar{\mathbf{q}}) e^{i\bar{\mathbf{q}} \cdot \bar{\mathbf{r}}}, \quad (\text{A10})$$

where the sum is over all co-deforming wave vectors $\bar{\mathbf{q}} = (\bar{q}_x, \bar{q}_y)$ with $\bar{q}_i = 2\pi n_i/L_i(0)$, where $n_i \in \mathbb{Z}$ and $i \in \{x, y\}$. A co-deforming Fourier mode with wave vector $\bar{\mathbf{q}}$ is distorted over time by the overall system deformation:

$$q_x(\bar{\mathbf{q}}, t) = l_x^{-1}(t) \bar{q}_x \quad (\text{A11})$$

$$q_y(\bar{\mathbf{q}}, t) = l_x(t) \bar{q}_y. \quad (\text{A12})$$

As in Eq. (A10), we have the usual derivation rule, where the Fourier transform of $\bar{\partial}_j f(\bar{\mathbf{r}}, \bar{t})$ is $i\bar{k}_j f(\bar{\mathbf{q}}, \bar{t})$. From Eqs. (A10) and (A1), it also follows that a given co-deforming Fourier mode with wave vector $\bar{\mathbf{q}}$ corresponds to a lab-frame Fourier mode with wave vector \mathbf{q} with components

$$q_i = \bar{q}_j s_{ji}^{-1}, \quad (\text{A13})$$

because then we have $\bar{\mathbf{q}} \cdot \bar{\mathbf{r}} = \mathbf{q} \cdot \mathbf{r}$.

Appendix B: Dynamics in co-deforming coordinates

Using Appendix A, we can express the dimensionless dynamic equations, Eqs. (10)–(13), in co-deforming coordinates:

$$\bar{\partial}_t s + \bar{v}_i (\bar{\partial}_i s) = 0 \quad (\text{B1})$$

$$\bar{\partial}_t c + \bar{v}_i (\bar{\partial}_i c) = (Ds_{ij}^{-2} \bar{\partial}_i \bar{\partial}_j - k_d) c + k_d s \quad (\text{B2})$$

$$0 = \frac{1}{4} s_{jl} \bar{\partial}_i^2 \bar{v}_l - \bar{\partial}_j \Pi + \bar{\partial}_i \tilde{\sigma}_{ij}^a \quad (\text{B3})$$

$$s_{il} \bar{\partial}_i \bar{v}_l = 0, \quad (\text{B4})$$

where $\tilde{\sigma}_{ij}^a$ is given by Eq. (6). Eqs. (B3) and (B4) are still expressed using lab-frame derivatives, because this will allow for a more convenient solution of the non-affine flows in the next section.

Finally, the system size dynamics for the freely deforming system, Eq. (7), becomes:

$$\frac{dl_x}{dt} = -\text{sgn}(\alpha)l_x \iint \left[l_x^{-2}(\bar{\partial}_x c)^2 - l_x^2(\bar{\partial}_y c)^2 \right] d\bar{x} d\bar{y}, \quad (\text{B5})$$

where the integral is over the box at time point 0, i.e. the integration variables are the co-deforming coordinates \bar{x} and \bar{y} .

1. Non-affine flows

For deforming systems, we will generally consider the dynamics of source and signaling fields in co-deforming coordinates, Eqs. (B1) and (B2). To obtain the non-affine flows, we solve Eqs. (B3) and (B4) by taking the lab-frame Fourier transform, which yields after some transformations:

$$\bar{v}_k = \frac{4is_{ki}^{-1}q_l}{q^2} \left(\delta_{ij} - \frac{q_i q_j}{q^2} \right) \bar{\sigma}_{lj}^a \quad (\text{B6})$$

with $\bar{\sigma}_{ij}^a$ given by Eq. (6).

Note that Eq. (B6) is undefined for $\mathbf{q} = 0$. Indeed, any constant homogeneous velocity can always be added to the flow field. Here and in the following, we will ignore this, because it does not affect the physics in any way.

2. Absence of non-affine flows for $\partial_y c = 0$

If the signaling field c is homogeneous in y direction, i.e. $\partial_y c = \bar{\partial}_y c = 0$, then there are no non-affine flows, i.e. there are no flows in co-deforming coordinates, $\bar{v} = 0$. For fixed system dimensions, this corresponds to a complete absence of flows, $\mathbf{v} = 0$.

Formally, the absence of non-affine flows follows from Eq. (B6), which links \bar{v} in Fourier space to the stress tensor in Fourier space. From Eq. (6) we obtain for $\partial_y c = 0$, that $\bar{\sigma}_{xy}^a = 0$ everywhere, and $\bar{\sigma}_{xx}^a$ is independent of y . Thus, in Fourier space, $\bar{\sigma}_{xx}^a$ is nonzero only for wave vectors \mathbf{q} that have a vanishing y component, $q_y = 0$. Insertion in Eq. (B6) yields indeed $\bar{v} = 0$.

Appendix C: Linearized dynamics

1. In co-deforming real space coordinates

We perturb the system around the dynamic state $\vec{z}_0 = (s_0(\bar{\mathbf{r}}), c_0(\bar{\mathbf{r}}), l_{x0})$ to linear order, where s_0 and c_0 only depend on \bar{x} :

$$s(\bar{\mathbf{r}}) = s_0(\bar{x}) + \delta s(\bar{\mathbf{r}}), \quad (\text{C1})$$

$$c(\bar{\mathbf{r}}) = c_0(\bar{x}) + \delta c(\bar{\mathbf{r}}), \quad (\text{C2})$$

$$l_x = l_{x0} + \delta l_x. \quad (\text{C3})$$

Because c_0 only depends on \bar{x} , we also have in the state \vec{z}_0 that $\bar{\sigma}_{xy}^a = 0$ and there are no non-affine flows, $\bar{v} = 0$ (Appendix B 2).

Combining Eqs. (C1)–(C3) with Eqs. (B1), (B2), and (B5) yields the following linearized dynamics:

$$\bar{\partial}_t \delta s = -s'_0 \delta \bar{v}_x, \quad (\text{C4})$$

$$\bar{\partial}_t \delta c = -c'_0 \delta \bar{v}_x + k_d(\delta s - \delta c)$$

$$+ Ds_{ij}^{-2} \bar{\partial}_i \bar{\partial}_j \delta c - 2D(\bar{\partial}_x^2 c_0) \frac{\delta l_x}{l_{x0}^3}, \quad (\text{C5})$$

$$\frac{d\delta l_x(t)}{dt} = \frac{2\text{sgn}(\alpha)}{l_{x0}} \iint (\bar{\partial}_x^2 c_0) \delta c d\bar{x} d\bar{y} - \frac{dl_{x0}}{dt} \frac{\delta l_x}{l_{x0}}, \quad (\text{C6})$$

where we have introduced the notation $s'_0 := \bar{\partial}_x s_0$ and $c'_0 := \bar{\partial}_x c_0$, and we used a partial integration in the linearized l_x dynamics.

2. In co-deforming Fourier space coordinates

In co-deforming Fourier space, the linearized dynamics read:

$$\bar{\partial}_t \delta s = -s'_0 * \delta \bar{v}_x \quad (\text{C7})$$

$$\bar{\partial}_t \delta c = -c'_0 * \delta \bar{v}_x + k_d(\delta s - \delta c)$$

$$- Ds_{ij}^{-2} \bar{q}_i \bar{q}_j \delta c + 2D\bar{q}_x^2 c_0 \frac{\delta l_x}{l_{x0}^3}, \quad (\text{C8})$$

$$\frac{d\delta l_x(t)}{dt} = -\frac{2\text{sgn}(\alpha)}{l_{x0}} \sum_{\bar{q}} \bar{q}_x^2 c_0^\dagger \delta c - \frac{dl_{x0}}{dt} \frac{\delta l_x}{l_{x0}}. \quad (\text{C9})$$

Here s'_0 and c'_0 represent the co-deforming Fourier transforms of $\bar{\partial}_x s_0$ and $\bar{\partial}_x c_0$, respectively. Furthermore, to rewrite the δl_x dynamics, we have used Parseval's identity, where the dagger, \cdot^\dagger , denotes the complex conjugate. We have moreover used the following definition of convolution operator, $*$, in co-deforming Fourier space:

$$f(\bar{q}) * g(\bar{q}) := \sum_{\bar{q}'} f(\bar{q}') g(\bar{q} - \bar{q}'), \quad (\text{C10})$$

where the sum is over all co-deforming wave vectors $\bar{q}' = (\bar{q}'_x, \bar{q}'_y)$ with $\bar{q}'_i = 2\pi n'_i / L_i(0)$, where $n'_i \in \mathbb{Z}$ and $i \in \{x, y\}$. For a fixed system size, we ignore the δl_x dynamics and the δl_x term in the δc dynamics.

To close Eqs. (C7)–(C9), we still need to insert the x -component of non-affine flow field perturbation, $\delta \bar{v}_x$. For convenience, we will use *lab-frame* Fourier modes to compute $\delta \bar{v}_x$. Specifically, we use Eq. (B6), which expresses \bar{v} in terms of the active stress tensor $\bar{\sigma}_{ij}^a$. We obtain to linear order:

$$\delta \bar{v}_x(q, \phi) = \frac{4i \sin \phi}{ql_{x0}} \left[\sin 2\phi \delta \bar{\sigma}_{xx}^a - \cos 2\phi \delta \bar{\sigma}_{xy}^a \right], \quad (\text{C11})$$

where q and ϕ denote the amplitude and orientation, respectively, of the lab-frame wave vector $\mathbf{q} = q(\cos \phi, \sin \phi)$.

We further express $\delta\tilde{\sigma}_{ij}^a$ in terms of δc using Eq. (6). To linear order, in lab-frame Fourier space:

$$\delta\tilde{\sigma}_{xj}^a = \frac{i\text{sgn}(\alpha)}{l_{x0}} c'_0 * (q_j \delta c) \quad \text{for } j \in \{x, y\}. \quad (\text{C12})$$

The other two components of the symmetric traceless tensor $\delta\tilde{\sigma}_{ij}^a$ are obtained through the relations $\delta\tilde{\sigma}_{yy}^a = -\delta\tilde{\sigma}_{xx}^a$ and $\delta\tilde{\sigma}_{yx}^a = \delta\tilde{\sigma}_{xy}^a$. The convolution operator in lab-frame Fourier coordinates in Eq. (C12) is defined analogously to Eq. (C10) as:

$$f(\mathbf{q}) * g(\mathbf{q}) := \sum_{\mathbf{q}'} f(\mathbf{q}') g(\mathbf{q} - \mathbf{q}'), \quad (\text{C13})$$

where the sum is over all lab-frame wave vectors $\mathbf{q}' = (q'_x, q'_y)$ with $q'_i = 2\pi n'_i / L_i(t)$, where $n'_i \in \mathbb{Z}$ and $i \in \{x, y\}$.

Combining (C11) and (C12), we obtain:

$$\delta\bar{v}_x = -\frac{4\text{sgn}(\alpha) \sin \phi}{ql_{x0}^2} \left\{ \sin 2\phi \left[c'_0 * (q_x \delta c) \right] - \cos 2\phi \left[c'_0 * (q_y \delta c) \right] \right\}. \quad (\text{C14})$$

The system of equations, Eqs. (C7)–(C9), and (C14), is now closed.

3. Numerical solution

In the special case of a linear source profile, we can solve the linearized dynamics analytically, because the gradients of s_0 and c_0 are constant, and thus the convolutions in Eqs. (C7), (C8), and (C14) collapse to a simple scaling factor. However, in general this is not the case, and we need to solve the linearized dynamics numerically.

To numerically compute the convolutions in Eqs. (C7), (C8), and (C14), we need to take into account that the numerical real-space representations of our fields are spatially discretised. To discuss the main ideas, we will discuss here the case of a single spatial dimension, \bar{x} , in co-deforming coordinates. The generalisation to lab frame coordinates and/or several dimensions will be straightforward. Specifically, we consider the periodic interval $\bar{x} \in [-L_x(0)/2, +L_x(0)/2]$ to be discretised by N_x equal-length steps $\Delta\bar{x} = L_x(0)/N_x$, where N_x is an even integer. Any function $f(\bar{x})$ is represented by a set of numbers f_k with $k = -N_x/2, -N_x/2+1, \dots, 0, \dots, N_x/2-1$, such that $f_k = f(k\Delta\bar{x})$. As a consequence, the Fourier series are not infinite any more as in Eq. (A10), but instead cut off at some finite wave vectors. In particular, the numerical co-deforming Fourier transform of f is represented by a set of complex numbers \tilde{f}_j with $j = -N_x/2, -N_x/2+1, \dots, 0, \dots, N_x/2-1$, where $\tilde{f}_j = f(\bar{q}_x = j\bar{q}_0)$ with $\bar{q}_0 := 2\pi/L_x(0)$. Eq. (A10) then becomes:

$$f_k = \sum_{j=-N_x/2}^{N_x/2-1} \tilde{f}_j e^{2\pi i (jk/N_x)}, \quad (\text{C15})$$

where we used that $\bar{q}_0 \Delta\bar{x} = 2\pi/N_x$.

We define the convolution of two Fourier transforms, \tilde{f}_j and \tilde{g}_j as follows:

$$(\tilde{f} * \tilde{g})_j = \sum_{j'=-N_x/2}^{N_x/2-1} \tilde{f}_{j'} \tilde{g}_{j-j'} \quad (\text{C16})$$

for $j = -N_x/2, -N_x/2+1, \dots, 0, \dots, N_x/2-1$. Yet, we see that the index $j - j'$ of \tilde{g} can get outside of the range $-N_x/2, -N_x/2+1, \dots, N_x/2-1$. To prevent aliasing effects, we set $\tilde{g}_j \equiv 0$ whenever $j < -N_x/2$ or $j \geq N_x/2$. Note that this technique for de-aliasing is akin to the zero-padding method [60, 61], frequently used for spectral solvers.

To numerically solve the linearized dynamics, Eqs. (C7)–(C9), we use an exponential ansatz for the time dependence of the perturbations,

$$\delta s(\bar{q}, t) = \delta\hat{s}(\bar{q}) e^{\omega t} \quad (\text{C17})$$

$$\delta c(\bar{q}, t) = \delta\hat{c}(\bar{q}) e^{\omega t} \quad (\text{C18})$$

$$\delta l_x(t) = \delta\hat{l}_x e^{\omega t}. \quad (\text{C19})$$

Inserting this in Eqs. (C7)–(C9) yields an eigenvalue problem:

$$\omega \delta\hat{\vec{z}} = M \cdot \delta\hat{\vec{z}}, \quad (\text{C20})$$

where the components of $\delta\hat{\vec{z}}$ are $\delta\hat{l}_x$ and the values of $\delta\hat{s}(\bar{q})$ and $\delta\hat{c}(\bar{q})$ for all $N_x N_y$ discrete values of the co-deforming wave vector \bar{q} . Thus, $\delta\hat{\vec{z}}$ has $2N_x N_y + 1$ components. The matrix M usually couples not only $\delta\hat{s}$ and $\delta\hat{c}$ components for the same wave vector \bar{q} to each other, but due to the convolutions in Eqs. (C7), (C8), and (C14), there is also mixing occurring across different wave vectors.

Appendix D: Fixed-size system with linear source

For linear source and signaling fields, the active flows, Eq. (C14), simplify to:

$$\delta v_x = -\omega_{\text{act}} \delta c \quad (\text{D1})$$

with

$$\omega_{\text{act}} = 4\text{sgn}(\alpha) \sin^2 \phi, \quad (\text{D2})$$

where ω_{act} is the perturbation growth rate for the case of a boundary-provided gradient without source field [35]. With this, the linearized dynamics, Eqs. (C7)–(C8) become:

$$\partial_t \delta s = \omega_{\text{act}} \delta c, \quad (\text{D3})$$

$$\partial_t \delta c = [\omega_{\text{act}} - Dq^2 - k_d] \delta c + k_d \delta s. \quad (\text{D4})$$

Thus, the convolutions in Eqs. (C7), (C8), and (C14) collapse to a constant prefactor. As a consequence, the solutions of the system are Fourier modes. In the following, we first discuss the limiting case of no diffusion before presenting the general solution.

1. No diffusion, $D = 0$

To solve the eigenvalue problem in this case, we define

$$\delta\Delta = \delta c - \delta s \quad (\text{D5})$$

$$\delta c_{\text{eff}} = \delta c + \frac{k_d}{\omega_{\text{act}}} \delta s. \quad (\text{D6})$$

Inserting this into Eqs. (D3) and (D4), we obtain:

$$\partial_t \delta\Delta = -k_d \delta\Delta \quad (\text{D7})$$

$$\partial_t \delta c_{\text{eff}} = \omega_{\text{act}} \delta c_{\text{eff}}. \quad (\text{D8})$$

Hence, the difference between both signaling and source, $\delta\Delta$, decays at rate k_d , while a superposition of both, δc_{eff} , grows with the same growth rate as the system without source [35].

2. General case

With an exponential Ansatz, where $\delta s \sim \delta c \sim e^{\omega t}$, we obtain an eigenvalue problem, whose solutions in ω are:

$$\omega_{\pm} = \frac{1}{2} \left[\mathcal{T} \pm \sqrt{\mathcal{T}^2 + 4k_d \omega_{\text{act}}} \right], \quad (\text{D9})$$

where $\mathcal{T} = \omega_{\text{act}} - Dq^2 - k_d$. The corresponding eigenvectors in $(\delta s, \delta c)$ are

$$\mathbf{v}_+ = \begin{pmatrix} \omega_+ \\ \omega_{\text{act}} \end{pmatrix} \quad \text{and} \quad \mathbf{v}_- = \begin{pmatrix} \omega_- \\ \omega_{\text{act}} \end{pmatrix}, \quad (\text{D10})$$

respectively.

Appendix E: Fixed-size system with localized source

1. Value of s_b in dimensionless units

As we discussed in section II C, we set the value of s_b such that the magnitude of the deformation rate of a system with $L_x = L_y = 1$ is one. This means that we set

$$s_b = \left[\sum_{q_x} \frac{k_d^2 |m(q_x)|^2}{(k_d + Dq_x^2)^2} \right]^{-1/2} \quad (\text{E1})$$

where $m(q_x)$ is the Fourier transform of the function

$$m(x) = \exp \left(\frac{\cos(q_0 x)}{(q_0 w)^2} \right) \quad (\text{E2})$$

which is defined on the interval $x \in [-1/2, 1/2]$, and where $q_0 = 2\pi/L_x$. Indeed, using Eqs. (7) and (22), one obtains that with the value of s_b from Eq. (E1), a von Mises source profile, Eq. (21), and $L_x = L_y = 1$, the absolute value of the shear rate is one.

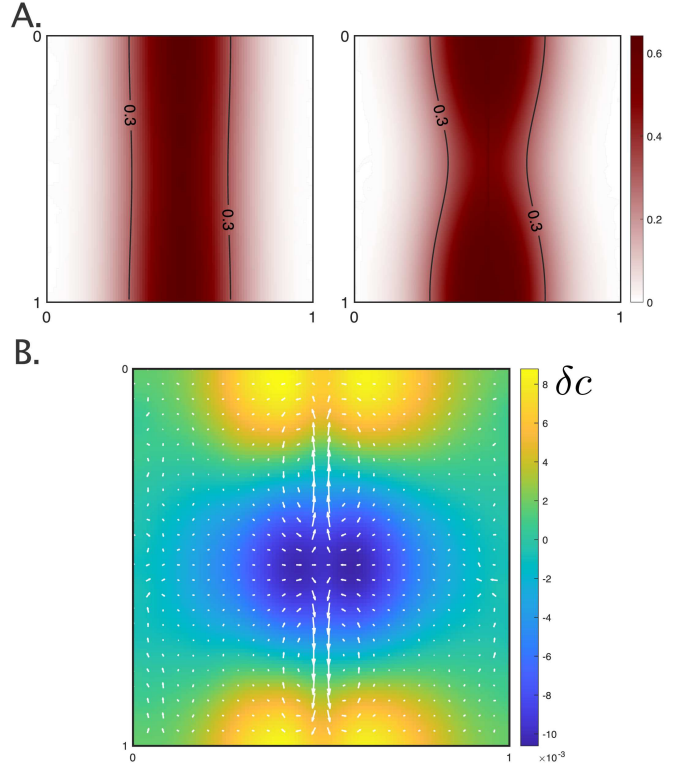


FIG. 5. Instability in a gradient-extensile system with fixed size and a localized source profile. (A) Snapshots of the late-time dynamics of the system in Figure 3C, showing the source profile at $t = 300$ (left) and $t = 1500$ (right). (B) Perturbation mode with maximum growth rate for system from Figure 3C and panel A. The color plot shows the signaling molecule perturbation, δc , and white arrows show the flow field perturbation, $\delta \mathbf{v}$.

2. Convergence to a finite perturbation growth rate for $D \rightarrow \infty$

The large-diffusion limit can be understood similarly to section III, where we assume that Dq_{\min}^2 is faster than any other rate to eliminate the signaling perturbation dynamics. Specifically, only the source perturbation dynamics, Eq. (C7), remains, where the signaling perturbation δc depends directly on the source perturbation through Eq. (19), which implies $\delta c \sim D^{-1} \delta s$. Moreover, for large D , Eq. (22) implies that $c_0 \sim D^{-1} s_0$, and thus $c'_0 \sim D^{-1} s'_0$.

In dimensionless units, we set s_b such that the free deformation rate is one, which implies $s_0 \sim s_b \sim D$ (compare Eq. (E1)). Thus, we have $c'_0 \sim D^0$. As a consequence, the perturbation of active stresses and active flows scale as $\delta \bar{v}_x \sim \delta \tilde{\sigma}_{ij}^a \sim c'_0 \delta c \sim D^{-1}$ (compare Eqs. (C12) and (C14)). The active flows enter in the advective term of the source field, Eq. (C7), where they are multiplied with the stationary source field, which scales as $s'_0 \sim s_b \sim D$. Hence, in the large- D limit, the source dynamics does not depend on D any more. As a conse-

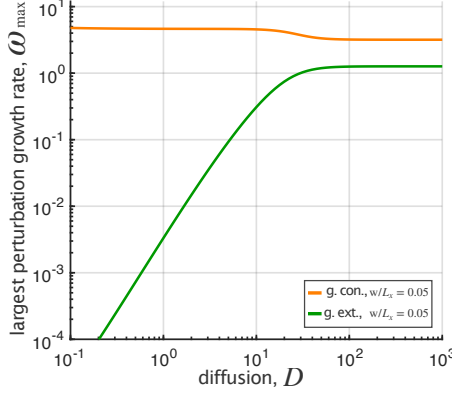


FIG. 6. Largest perturbation growth rates ω_{\max} of a fixed-size system as a function of the signaling molecule diffusion. Parameter values, $k_d = 1$ and $L_x = L_y = 1$.

quence, the largest perturbation growth rate is constant.

In dimensionful units, i.e. if we imposed a constant source magnitude $s_b \sim D^0$, we would have $c'_0 \sim D^{-1}$. Hence, the perturbation growth rate would scale as $c'_0 \delta c \sim D^{-2}$, and the free deformation rate would scale as $\tilde{\sigma}_{xx}^a \sim (c'_0)^2 \sim D^{-2}$. Hence, the perturbation growth rate decreases with D in the same way as the free deformation rate.

Appendix F: Deforming system with localized source

1. System dimension dynamics

The dynamics of system dimension L_x , and thus box shear l_x , is given by Eq. (7).

We first discuss the case without diffusion, $D = 0$, where source and signaling fields, $s(\bar{x})$ and $c(\bar{x})$, are stationary in co-deforming coordinates. In this case, the shear rate is essentially given by the integral over $(\partial_x c_0)^2$. Because the signaling profile, c_0 , is stationary in co-deforming coordinates, we have that for varying system size, $(\partial_x c_0)^2 \sim 1/l_x^2 (\bar{\partial}_x c_0)^2 \sim 1/l_x^2$. So, using dimensionless units (section II C), we can write

$$\frac{1}{l_x} \frac{dl_x}{dt} = -\frac{\text{sgn}(\alpha)}{L_x^2(0)l_x^2}. \quad (\text{F1})$$

The solution of this is:

$$l_x(t) = \sqrt{1 - \frac{2\text{sgn}(\alpha)t}{L_x^2(0)^2}}. \quad (\text{F2})$$

Thus, gradient-extensile systems ($\alpha < 0$) deform more and more slowly over time due to the widening of the signaling profile (green curves in Figure 7A). Meanwhile, gradient-contractile systems ($\alpha > 0$) deform faster and faster over time due to the compression of the signaling profile, until the deformation rate diverges at some

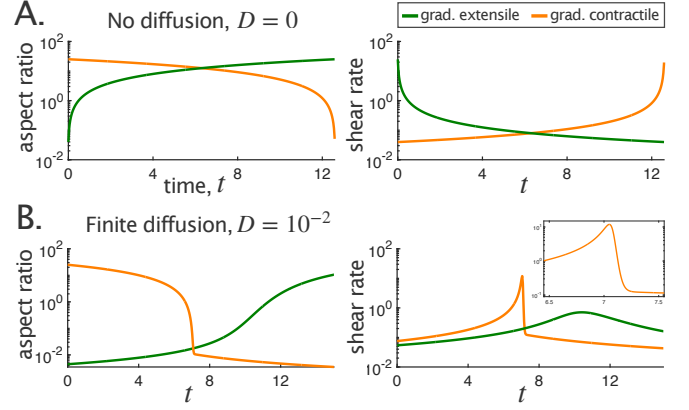


FIG. 7. System size dynamics of a freely deforming system in the limit $w \rightarrow \infty$, where the source has a cosine shape. Here, $k_d = 1$. (A) Aspect ratios (left) and shear rates (right) over time for the gradient-extensile (green) and contractile (orange) systems, starting at initial aspect ratios of $L_x(0)/L_y(0) = 1/225$ and $L_x(0)/L_y(0) = 25$, respectively. Here the signaling molecule is non-diffusive, $D = 0$. (B) The same data as panel A shown for a system with diffusive signaling molecule with $D = 10^{-2}$. Here, the gradient-extensile (green) and gradient-contractile (orange) systems start from $L_x(0)/L_y(0) = 0.04$ and $L_x(0)/L_y(0) = 25$, respectively. Inset: zoomed around the sharp drop in the gradient-contractile case.

critical time point $t_{\text{crit}} = L_x^2(0)/2$ (orange curves in Figure 7A).

This box dimension dynamics is changed when allowing for finite diffusion, $D > 0$ (Figure 7B). Specifically, the shear rate of gradient-extensile systems first increases, before it decreases like in the case without diffusion (compare green curves in Figure 7A,B, right panels). In gradient contractile systems, the shear rate first increases, like in the case without diffusion before it rather abruptly drops (compare orange curves in Figure 7A,B right panels and Figure 7B inset).

To better understand these effects of diffusion, we first note that without any non-affine flows (i.e. $\bar{\mathbf{v}} = \mathbf{0}$), both signaling and source profiles keep their cosine profiles, $s(\mathbf{r}, t) = \hat{s}[\cos(2\pi x/L_x) + 1]$ and $c(\mathbf{r}, t) = \hat{c}(t) \cos(2\pi x/L_x) + c_{\text{offset}}(t)$, while only the signaling amplitude $\hat{c}(t)$ and offset $c_{\text{offset}}(t)$ vary over time. We can thus simplify the dynamics to:

$$\frac{d\hat{c}}{dt} = -k_d(\hat{c} - \hat{s}) - 4\pi^2 D \frac{\hat{c}}{L_x^2(0)l_x^2} \quad (\text{F3})$$

$$\frac{1}{l_x} \frac{dl_x}{dt} = -\frac{2\pi^2 \text{sgn}(\alpha) \hat{c}^2}{L_x^2(0)l_x^2}, \quad (\text{F4})$$

where \hat{s} is constant since $\bar{\mathbf{v}} = \mathbf{0}$, and the offset $c_{\text{offset}}(t)$ does not matter for the box dimension dynamics. Eq. (F4) implies that the shear rate scales as $\sim \hat{c}^2/l_x^2$. Further, the diffusion term in Eq. (F3) can be neglected as long as $l_x \gtrsim \sqrt{D/k_d}/L_x(0)$, and consequently $\hat{c} \simeq \hat{s}$. In other words, the box shear rate

for large l_x is the same as in the case without diffusion, where the shear rate scales as $\sim l_x^{-2}$, for both gradient-extensile and gradient-contractile systems, consistent with Figure 7A,B. Conversely, taking Eq. (F3) to the adiabatic limit of large diffusion D and/or small box shear l_x , we have $\hat{c} \sim (k_d/D)L_x^2(0)l_x^2\hat{s} \sim l_x^2$. Thus, in the limit of small box shear l_x , the shear rate scales as $\sim \hat{c}^2/l_x^2 \sim l_x^2$, i.e. it increases with l_x , again consistent with Figure 7A,B.

2. Affine diffusion-shear instability

To discuss the affine diffusion-shear instability, we start from the linearized dynamics in Fourier space, Eqs. (C7)–(C9), where we set non-affine flows to zero, $\delta\bar{\mathbf{v}} = 0$, we ignore any variations of the source field, $\delta s = 0$, and we ignore any y -dependence of the perturbations. We obtain from Eqs. (C8) and (C9) with an exponential Ansatz for the time dependency, $\delta c(\bar{q}_x, t) = \delta\tilde{c}(\bar{q}_x)e^{\omega t}$ and $\delta l_x(t) = \delta\tilde{l}_x e^{\omega t}$:

$$\omega\delta\tilde{c}(\bar{q}_x) = -k_d(1 + \lambda^2 q_x^2)\delta\tilde{c}(\bar{q}_x) + 2k_d\lambda^2 q_x^2 c_0(\bar{q}_x) \frac{\delta\tilde{l}_x}{l_x} \quad (\text{F5})$$

$$\begin{aligned} \omega \frac{\delta\tilde{l}_x}{l_x} &= -2\text{sgn}(\alpha) \sum_{\bar{q}_x} q_x^2 c_0^\dagger(\bar{q}_x) \delta\tilde{c}(\bar{q}_x) \\ &\quad + \text{sgn}(\alpha) \frac{\delta\tilde{l}_x}{l_x} \sum_{\bar{q}_x} q_x^2 |c_0(\bar{q}_x)|^2. \end{aligned} \quad (\text{F6})$$

Here, we also substituted the diffusion length scale $\lambda = \sqrt{D/k_d}$ and the lab-frame wave vector $q_x = \bar{q}_x/l_x$. If this linear system of equations has a positive eigenvalue ω , then there is an instability.

a. Cosine source profile

For the case of a cosine profile, the only nonzero values of $c_0(\bar{q}_x)$ are $c_0 \equiv c_0(\pm\bar{q}_0)$ with $\bar{q}_0 = 2\pi/L_x(0)$. Then, Eqs. (F5) and (F6) become:

$$\omega\delta\tilde{c} = -k_d(1 + \lambda^2 q_0^2)\delta\tilde{c} + 2k_d\lambda^2 q_0^2 c_0 \frac{\delta\tilde{l}_x}{l_x} \quad (\text{F7})$$

$$\omega \frac{\delta\tilde{l}_x}{l_x} = -4\text{sgn}(\alpha)q_0^2 c_0^\dagger \delta\tilde{c} + 2\text{sgn}(\alpha)q_0^2 |c_0|^2 \frac{\delta\tilde{l}_x}{l_x}, \quad (\text{F8})$$

where $q_0(t) := \bar{q}_0/l_x(t) = 2\pi/L_x(t)$. There are two eigenvalues, ω_1 and ω_2 with $\omega_1 \leq \omega_2$, and the largest is given by:

$$\omega_2 = \frac{1}{2} \left[\mathcal{T} + \sqrt{\mathcal{T}^2 - 4\mathcal{D}} \right], \quad (\text{F9})$$

where $\mathcal{T} := -k_d(1 + \lambda^2 q_0^2) + 2\text{sgn}(\alpha)q_0^2 |c_0|^2$ and $\mathcal{D} := -2\text{sgn}(\alpha)k_d q_0^2 |c_0|^2 (1 - 3\lambda^2 q_0^2)$ are trace and determinant,

respectively, of the matrix on the right-hand side of Eqs. (F7) and (F8).

In the gradient-extensile case, $\text{sgn}(\alpha) = -1$, we have that $\omega_1 + \omega_2 = \mathcal{T} < 0$. Thus, at least one eigenvalue is negative. The product of both eigenvalues is given by $\omega_1\omega_2 = \mathcal{D} = 2k_d q_0^2 |c_0|^2 (1 - 3\lambda^2 q_0^2)$. Hence, there is a positive eigenvalue iff $3\lambda^2 q_0^2 > 1$, i.e. iff $2\pi\lambda\sqrt{3} > L_x$.

b. Arbitrary source profile

For the case of an arbitrary source profile s_0 , we focus on the gradient-extensile case, $\text{sgn}(\alpha) = -1$. We discuss the existence of positive solutions ω by first expressing $\delta\tilde{c}(\bar{q}_x)$ in terms of $\delta\tilde{l}_x$ and ω using Eq. (F5):

$$\delta\tilde{c}(\bar{q}_x) = \frac{2\lambda^2 q_x^2 c_0(\bar{q}_x)}{1 + \omega/k_d + \lambda^2 q_x^2} \frac{\delta\tilde{l}_x}{l_x}. \quad (\text{F10})$$

Insertion into Eq. (F6) yields:

$$\begin{aligned} \omega &= \sum_{\bar{q}_x} q_x^2 |c_0(\bar{q}_x)|^2 \frac{4\lambda^2 q_x^2}{1 + \omega/k_d + \lambda^2 q_x^2} - \sum_{\bar{q}_x} q_x^2 |c_0(\bar{q}_x)|^2 \\ &= \sum_{\bar{q}_x} q_x^2 |c_0(\bar{q}_x)|^2 \frac{3\lambda^2 q_x^2 - 1 - \omega/k_d}{1 + \omega/k_d + \lambda^2 q_x^2}. \end{aligned} \quad (\text{F11})$$

To solve this self-consistent equation for ω , we look for the zeros of the function

$$f_\lambda(\omega) := -\omega + \sum_{\bar{q}_x} q_x^2 |c_0(\bar{q}_x)|^2 \frac{3\lambda^2 q_x^2 - 1 - \omega/k_d}{1 + \omega/k_d + \lambda^2 q_x^2}. \quad (\text{F12})$$

Specifically, we now show that iff $f_\lambda(0) > 0$, there exists a positive solution in ω , i.e. an $\omega > 0$ for which $f_\lambda(\omega) = 0$. This means that there is an affine diffusion-shear instability iff $f_\lambda(0) > 0$. To show this, we first assume that there is an $\omega > 0$ for which $f_\lambda(\omega) = 0$. Then, we have:

$$\begin{aligned} 0 &< \omega \\ &= \sum_{\bar{q}_x} q_x^2 |c_0(\bar{q}_x)|^2 \frac{3\lambda^2 q_x^2 - 1 - \omega/k_d}{1 + \omega/k_d + \lambda^2 q_x^2} \\ &< \sum_{\bar{q}_x} q_x^2 |c_0(\bar{q}_x)|^2 \frac{3\lambda^2 q_x^2 - 1}{1 + \lambda^2 q_x^2} \\ &= f_\lambda(0). \end{aligned} \quad (\text{F13})$$

In these transformations, we have subsequently used $\omega > 0$, $f_\lambda(\omega) = 0$, $\omega > 0$, and the definition of $f_\lambda(\omega)$. Thus, if there is an $\omega > 0$ for which $f_\lambda(\omega) = 0$, then $f_\lambda(0) > 0$.

Second, we assume that $f_\lambda(0) > 0$. To show that there is a positive zero of f_λ , we need to show that there is a positive $\hat{\omega} > 0$ for which $f_\lambda(\hat{\omega}) < 0$. Then, the Intermediate Value Theorem implies that there is an ω with $0 < \omega < \hat{\omega}$ such that $f_\lambda(\omega) = 0$. Indeed, for

$\hat{\omega} = 3 \sum_{\bar{q}_x} q_x^2 |c_0(\bar{q}_x)|^2$, we find that:

$$\begin{aligned}
f_\lambda(\hat{\omega}) &= -3 \sum_{\bar{q}_x} q_x^2 |c_0(\bar{q}_x)|^2 \\
&\quad + \sum_{\bar{q}_x} q_x^2 |c_0(\bar{q}_x)|^2 \frac{3\lambda^2 q_x^2 - 1 - \hat{\omega}/k_d}{1 + \hat{\omega}/k_d + \lambda^2 q_x^2} \\
&= \sum_{\bar{q}_x} q_x^2 |c_0(\bar{q}_x)|^2 \frac{-2(1 + \hat{\omega}/k_d)}{1 + \hat{\omega}/k_d + \lambda^2 q_x^2} \\
&< 0.
\end{aligned} \tag{F14}$$

Thus, if $f_\lambda(0) > 0$ then f_λ has a positive zero and the affine diffusion-shear instability exists. Taken together, the sign of $f_\lambda(0)$ directly indicates the existence of an instability.

Finally, we discuss the sign of $f_\lambda(0)$. Using Eq. (22), we can express $f_\lambda(0)$ in terms of the source profile:

$$f_\lambda(0) = \frac{1}{\lambda^2} \sum_{\bar{q}_x} |s_0(\bar{q}_x)|^2 \frac{\lambda^2 q_x^2 (3\lambda^2 q_x^2 - 1)}{(1 + \lambda^2 q_x^2)^3}. \tag{F15}$$

Choosing for s_0 the von Mises profile in Eq. (21) with finite width w , we numerically obtain $f_\lambda(0) > 0$ iff $\lambda > gw$ with $g \approx 0.639$ in the limit where $w \ll L_x$ (i.e. where the von Mises profile becomes a Gaussian with standard deviation w). However, the precise value of g depends on the shape of the profile s_0 . For a rectangular profile of s_0 , we numerically even find that the instability always occurs.

Appendix G: Non-linearity in the active stress

We consider the system of equations, Eqs. (1)–(6), where we introduce a non-linearity into the active stress, Eq. (6):

$$\tilde{\sigma}_{ij}^a = \alpha h([\partial_k c]^2) \left[(\partial_i c)(\partial_j c) - \frac{1}{2} (\partial_k c)^2 \delta_{ij} \right], \tag{G1}$$

where $z \mapsto h(z)$ is some real function expressing the non-linearity. In the following, we assume that $h(z) > 0$ for any real z , and that the function $z \mapsto zh(z)$ is monotonously increasing, i.e. the magnitude of the active stress increases monotonously with the magnitude of scalar field gradient.

Then, the dimensionless, linearized dynamics become:

$$\bar{\partial}_t \delta s = -s'_0 \delta \bar{v}_x, \tag{G2}$$

$$\begin{aligned}
\bar{\partial}_t \delta c &= -c'_0 \delta \bar{v}_x + k_d (\delta s - \delta c) \\
&\quad + D s_{ij}^{-2} \bar{\partial}_i \bar{\partial}_j \delta c - 2D (\bar{\partial}_x^2 c_0) \frac{\delta l_x}{l_{x0}^3}, \tag{G3}
\end{aligned}$$

$$\begin{aligned}
\frac{d\delta l_x(t)}{dt} &= -2 \operatorname{sgn}(\alpha) \iint [h(z) + zh'(z)] \frac{c'_0}{l_{x0}} \delta c' d\bar{x} d\bar{y} \\
&\quad + \operatorname{sgn}(\alpha) (I_0 + 2\Delta I) \delta l_x, \tag{G4}
\end{aligned}$$

where $\delta c' := \bar{\partial}_x \delta c$, and

$$I_0 := \iint z h(z) d\bar{x} d\bar{y} \tag{G5}$$

$$\Delta I := \iint z^2 h'(z) d\bar{x} d\bar{y} \tag{G6}$$

with $z(\bar{r}) := (c'_0(\bar{x})/l_{x0})^2$.

We further focus on the gradient-extensile case, $\operatorname{sgn}(\alpha) = -1$, without non-affine flows, $\bar{v} = \mathbf{0}$, and, for simplicity, we consider the limit $w \rightarrow \infty$, such that $s_0(\bar{x}) \sim \cos(\bar{q}_0 \bar{x})$, and thus also $c_0(\bar{x}) = \hat{c}_0 \cos(\bar{q}_0 \bar{x})$ with $\bar{q}_0 = 2\pi/L_x(0)$ and some constant prefactor \hat{c}_0 . As a consequence, based on Eq. (G3), all Fourier modes of δc decay except for $\delta c = \hat{\delta} \hat{c} \cos(\bar{q}_0 \bar{x})$. Hence, $\delta c(\bar{x}) = (\hat{\delta} \hat{c} / \hat{c}_0) c_0(\bar{x})$. As a consequence, Eqs. (G3) and (G4) simplify to:

$$\frac{d\hat{\delta} \hat{c}}{dt} = -(k_d + Dq_0^2) \hat{\delta} \hat{c} + 2Dq_0^2 \hat{c}_0 \frac{\delta l_x}{l_{x0}}, \tag{G7}$$

$$\frac{d\delta l_x(t)}{dt} = 2(I_0 + \Delta I) l_{x0} \frac{\hat{\delta} \hat{c}}{\hat{c}_0} - (I_0 + 2\Delta I) \delta l_x. \tag{G8}$$

This is a linear system of differential equations with constant coefficients. It is linearly stable if both eigenvalues, ω_1 and ω_2 , of the coefficient matrix are negative. This implies that the trace of the matrix needs to be negative: $0 > \omega_1 + \omega_2 = -k_d - Dq_0^2 - I_0 - 2\Delta I$, and that the determinant of the matrix needs to be positive: $0 < \omega_1 \omega_2 = (k_d + Dq_0^2)(I_0 + 2\Delta I) - 4Dq_0^2(I_0 + \Delta I) = k_d(I_0 + 2\Delta I) - Dq_0^2(3I_0 + 2\Delta I)$. For the system to be stable also for large diffusion, i.e. for $k_d \ll Dq_0^2$, the latter condition implies $-3I_0 - 2\Delta I > 0$. However, we have assumed that $h(z) > 0$, implying $I_0 > 0$, and that $z \mapsto zh(z)$ increases monotonically, implying that $h(z) + zh'(z) \geq 0$ and thus $I_0 + \Delta I \geq 0$. This contradicts determinant condition for a stable system. Taken together, this means that the diffusion-shear instability arises for large diffusion for any non-linearity h in the active stress. We expect this result to generalize also to finite source widths w ; higher-order Fourier modes in c_0 would increase prefactor of the first term in Eq. (G8), and thus make the system more unstable.

[1] L. Wolpert, C. Tickle, and A. M. Arias, *Principles of Development* (Oxford University Press, 2015).

[2] J. A. Zallen and E. Wieschaus, Patterned Gene Expression Directs Bipolar Planar Polarity in *Drosophila*, *Dev. Cell* **6**, 343 (2004).

[3] B. Bénazéraf, P. Francois, R. E. Baker, N. Denans, C. D. Little, and O. Pourquié, A random cell motility gradient downstream of FGF controls elongation of an amniote embryo, *Nature* **466**, 248 (2010).

[4] A. Shindo, Models of convergent extension during morphogenesis, *Wiley Interdisciplinary Reviews: Developmental Biology* **7**, 10.1002/wdev.293 (2018).

[5] K. A. Johansen, D. D. Iwaki, and J. A. Lengyel, Localized JAK/STAT signaling is required for oriented cell rearrangement in a tubular epithelium, *Development* **130**, 135 (2003).

[6] C. M. Karner, R. Chirumamilla, S. Aoki, P. Igarashi, J. B. Wallingford, and T. J. Carroll, Wnt9b signaling regulates planar cell polarity and kidney tubule morphogenesis, *Nature Genetics* **41**, 793 (2009).

[7] A. Saxena, B. Denholm, S. Bunt, M. Bischoff, K. VijayRaghavan, and H. Skaer, Epidermal Growth Factor Signalling Controls Myosin II Planar Polarity to Orchestrate Convergent Extension Movements during *Drosophila* Tubulogenesis, *PLoS Biology* **12**, 1002013 (2014).

[8] R. Etournay, M. Popović, M. Merkel, A. Nandi, C. Blasse, B. Aigouy, H. Brandl, G. Myers, G. Salbreux, F. Jülicher, and S. Eaton, Interplay of cell dynamics and epithelial tension during morphogenesis of the *Drosophila* pupal wing, *eLife* **4**, e07090 (2015).

[9] S. Hopyan, Biophysical regulation of early limb bud morphogenesis, *Developmental Biology* **429**, 429 (2017).

[10] H. Tao, M. Zhu, K. Lau, O. K. W. Whitley, M. Samani, X. Xiao, X. X. Chen, N. A. Hahn, W. Liu, M. Valencia, M. Wu, X. Wang, K. D. Fenelon, C. C. Pasiliao, D. Hu, J. Wu, S. Spring, J. Ferguson, E. P. Karuna, R. M. Henkelman, A. Dunn, H. Huang, H.-Y. H. Ho, R. Atit, S. Goyal, Y. Sun, and S. Hopyan, Oscillatory cortical forces promote three dimensional cell intercalations that shape the murine mandibular arch, *Nature Communications* **10**, 1703 (2019).

[11] C. Bertet, L. Sulak, and T. Lecuit, Myosin-dependent junction remodelling controls planar cell intercalation and axis elongation, *Nature* **429**, 667 (2004).

[12] F. Bosveld, I. Bonnet, B. Guirao, S. Tlili, Z. Wang, A. Petitallot, R. Marchand, P.-L. Bardet, P. Marcq, F. Graner, and Y. Bellaïche, Mechanical Control of Morphogenesis by Fat/Dachsous/Four-Jointed Planar Cell Polarity Pathway, *Science (80-.).* **336**, 724 (2012).

[13] C. Collinet, M. Rauzi, P. F. Lenne, and T. Lecuit, Local and tissue-scale forces drive oriented junction growth during tissue extension, *Nature Cell Biology* **17**, 1247 (2015).

[14] M. Behrndt, G. Salbreux, P. Campinho, R. Hauschild, F. Oswald, J. Roensch, S. W. Grill, and C. P. Heisenberg, Forces driving epithelial spreading in zebrafish gastrulation, *Science* **338**, 257 (2012).

[15] S. J. Streichan, M. Lefebvre, N. Noll, E. F. Wieschaus, and B. I. Shraiman, Global morphogenetic flow is accurately predicted by the spatial distribution of myosin motors, *eLife* **7**, e27454 (2018).

[16] A. Stokkermans, A. Chakrabarti, K. Subramanian, L. Wang, S. Yin, P. Moghe, P. Steenbergen, G. Mönke, T. Hiramatsu, R. Prevedel, L. Mahadevan, and A. Ikmı, Muscular hydraulics drive larva-polyp morphogenesis, *Current Biology* **32**, 4707 (2022).

[17] E. W. Gehrels, B. Chakrabortty, M.-E. Perrin, M. Merkel, and T. Lecuit, Curvature gradient drives polarized tissue flow in the *Drosophila* embryo, *Proceedings of the National Academy of Sciences* **120**, e2214205120 (2023).

[18] N. A. Dye, M. Popovic, K. V. Iyer, J. F. Fuhrmann, R. Piscitello-Gómez, S. Eaton, and F. Julicher, Self-organized patterning of cell morphology via mechanosensitive feedback, *eLife* **10**, 10.7554/ELIFE.57964 (2021).

[19] M. Serra, G. S. Nájera, M. Chuai, A. M. Plum, S. Santosh, V. Spandan, C. J. Weijer, and L. Mahadevan, A mechanochemical model recapitulates distinct vertebrate gastrulation modes, *Science advances* **9**, eadh8152 (2023).

[20] S. Gsell, S. Tlili, M. Merkel, and P.-F. Lenne, Marangoni-like tissue flows enhance symmetry breaking of embryonic organoids, *bioRxiv* **10.1101/2023.09.22.559003** (2024).

[21] K. Barrett, S. Anand, V. Thome, P.-F. Lenne, and M. Merkel, Epithelial-mesenchymal boundary guides cell shapes and axis elongation in embryonic explants, *bioRxiv* **10.1101/2024.08.20.608779** (2024).

[22] N. H. Claussen, F. Brauns, and B. I. Shraiman, A geometric-tension-dynamics model of epithelial convergent extension, *Proceedings of the National Academy of Sciences* **121**, e2321928121 (2024), <https://www.pnas.org/doi/pdf/10.1073/pnas.2321928121>.

[23] A. Ioratim-Uba, T. B. Liverpool, and S. Henkes, Mechanochemical active feedback generates convergence extension in epithelial tissue, *Physical Review Letters* **131**, 238301 (2023).

[24] R. A. Simha and S. Ramaswamy, Hydrodynamic fluctuations and instabilities in ordered suspensions of self-propelled particles, *Phys. Rev. Lett.* **89**, 058101 (2002), [arXiv:0108301v2 \[arXiv:cond-mat\]](https://arxiv.org/abs/0108301v2).

[25] R. Voituriez, J. F. Joanny, and J. Prost, Spontaneous flow transition in active polar gels, *Europhys. Lett.* **70**, 404 (2005), [arXiv:0503022 \[q-bio\]](https://arxiv.org/abs/0503022).

[26] M. C. Marchetti, J. F. Joanny, S. Ramaswamy, T. B. Liverpool, J. Prost, M. Rao, and R. A. Simha, Hydrodynamics of soft active matter, *Reviews of Modern Physics* **85**, 1143 (2013), [arXiv:1207.2929v1](https://arxiv.org/abs/1207.2929v1).

[27] S. von der Hardt, J. Bakkers, A. Inbal, L. Carvalho, L. Solnica-Krezel, C. P. Heisenberg, and M. Hammer, The Bmp Gradient of the Zebrafish Gastrula Guides Migrating Lateral Cells by Regulating Cell-Cell Adhesion, *Current Biology* **17**, 475 (2007).

[28] K. W. Rogers and A. F. Schier, Morphogen Gradients: From Generation to Interpretation, *Annual Review of Cell and Developmental Biology* **27**, 377.

[29] P. Müller, K. W. Rogers, S. R. Yu, M. Brand, and A. F. Schier, Morphogen transport, *Development (Cambridge)* **140**, 1621 (2013).

[30] G. Tkačík, J. O. Dubuis, M. D. Petkova, and T. Gregor, Positional Information, Positional Error, and Readout Precision in Morphogenesis: A Mathematical Framework, *Genetics* **199**, 39 (2015), [arXiv:1404.5599](https://arxiv.org/abs/1404.5599).

[31] L. S. Mosby, A. E. Bowen, and Z. Hadjivasiliou, Morphogens in the evolution of size, shape and patterning, *Development* **151**, dev202412.

[32] H. Ninomiya, R. P. Elinson, and R. Winklbauer, Antero-posterior tissue polarity links mesoderm convergent extension to axial patterning, *Nature* **430**, 364 (2004).

[33] J. Lavalou, Q. Mao, S. Harmansa, S. Kerridge, A. C. Lelouch, J. M. Philippe, S. Audebert, L. Camoin, and T. Lecuit, Formation of polarized contractile interfaces by self-organized Toll-8/Cirr GPCR asymmetry, *Dev. Cell* **56**, 1574 (2021).

[34] Z. Wang, M. C. Marchetti, and F. Brauns, Patterning of morphogenetic anisotropy fields, *Proceedings of the National Academy of Sciences of the United States of America* **120**, e2220167120 (2023), arXiv:2212.12215.

[35] M. Ibrahimi and M. Merkel, Deforming polar active matter in a scalar field gradient, *New Journal of Physics* **25**, 013022 (2023), arXiv:2206.12850.

[36] M. F. Lefebvre, N. H. Claussen, N. P. Mitchell, H. J. Gustafson, and S. J. Streichan, Geometric control of Myosin-II orientation during axis elongation, *eLife* **12**, 2022.01.12.476069 (2023).

[37] A. M. Plum and M. Serra, *Morphogen Patterning in Dynamic Tissues* (2025).

[38] O. Wartlick, P. Mumcu, A. Kicheva, T. Bittig, C. Seum, F. Jülicher, and M. González-Gaitán, Dynamics of Dpp signaling and proliferation control, *Science* **331**, 1154 (2011).

[39] R. Mateus, L. Holtzer, C. Seum, Z. Hadjivasiliou, M. Dubois, F. Jülicher, and M. Gonzalez-Gaitan, BMP Signaling Gradient Scaling in the Zebrafish Pectoral Fin, *Cell Reports* **30**, 4292 (2020).

[40] M. Romanova-Michaelides, Z. Hadjivasiliou, D. Aguilar-Hidalgo, D. Basagiannis, C. Seum, M. Dubois, F. Jülicher, and M. Gonzalez-Gaitan, Morphogen gradient scaling by recycling of intracellular Dpp, *Nature* **602**, 287 (2022).

[41] O. Wartlick, A. Kicheva, and M. González-Gaitán, Morphogen gradient formation., *Cold Spring Harbor perspectives in biology* **1**, 10.1101/cshperspect.a001255 (2009).

[42] Y. Wang, X. Wang, T. Wohland, and K. Sampath, Extracellular interactions and ligand degradation shape the nodal morphogen gradient, *eLife* **5**, 10.7554/eLife.13879 (2016).

[43] A. Huang, C. Amourda, S. Zhang, N. S. Tolwinski, and T. E. Saunders, Decoding temporal interpretation of the morphogen bicoid in the early drosophila embryo, *eLife* **6**, 1 (2017).

[44] A. C. Paré, A. Vichas, C. T. Fincher, Z. Mirman, D. L. Farrell, A. Mainieri, and J. A. Zallen, A positional Toll receptor code directs convergent extension in Drosophila, *Nature* **515**, 523 (2014).

[45] M. A. Benton, M. Pechmann, N. Frey, D. Stappert, K. H. Conrads, Y. T. Chen, E. Stamataki, A. Pavlopoulos, and S. Roth, Toll Genes Have an Ancestral Role in Axis Elongation, *Current Biology* **26**, 1609 (2016).

[46] D. Jia, Q. Xu, Q. Xie, W. Mio, and W. M. Deng, Automatic stage identification of Drosophila egg chamber based on DAPI images, *Scientific Reports* **6**, 1 (2016).

[47] H. Alégot, P. Pouchin, O. Bardot, and V. Mirouse, Jak-stat pathway induces Drosophila follicle elongation by a gradient of apical contractility, *eLife* **7**, 10.7554/eLife.32943 (2018).

[48] D. D. Iwaki, K. A. Johansen, J. B. Singer, and J. A. Lengyel, Drumstick, bowl, and lines are required for patterning and cell rearrangement in the Drosophila embryonic hindgut, *Developmental Biology* **240**, 611 (2001).

[49] M. L. Williams and L. Solnica-Krezel, Nodal and planar cell polarity signaling cooperate to regulate zebrafish convergence and extension gastrulation movements, *eLife* **9**, 10.7554/eLife.54445 (2020).

[50] B. Steventon, F. Duarte, R. Lagadec, S. Mazan, J. F. Nicolas, and E. Hirsinger, Species-specific contribution of volumetric growth and tissue convergence to posterior body elongation in vertebrates, *Development (Cambridge)* **143**, 1732 (2016).

[51] A. Kicheva, P. Pantazis, T. Bollenbach, Y. Kalaidzidis, T. Bittig, F. Jülicher, and M. González-Gaitán, Kinetics of morphogen gradient formation, *Science* **315**, 521 (2007).

[52] A. Tiribocchi, R. Wittkowski, D. Marenduzzo, and M. E. Cates, Active Model H: Scalar Active Matter in a Momentum-Conserving Fluid, *Phys. Rev. Lett.* **115**, 1 (2015), arXiv:1504.07447v1.

[53] T. R. Kirkpatrick and J. K. Bhattacherjee, Driven active matter: Fluctuations and a hydrodynamic instability, *Phys. Rev. Fluids* **4**, 1 (2019).

[54] B. Gao, Wnt Regulation of Planar Cell Polarity (PCP), *Current Topics in Developmental Biology* **101**, 263 (2012).

[55] M. Merkel, A. Sagner, F. S. Gruber, R. Etournay, C. Blasse, E. Myers, S. Eaton, and F. Jülicher, The balance of prickle/spiny-legs isoforms controls the amount of coupling between core and fat PCP systems, *Current Biology* **24**, 2111 (2014).

[56] S. S. Lienkamp, K. Liu, C. M. Karner, T. J. Carroll, O. Ronneberger, J. B. Wallingford, and G. Walz, Vertebrate kidney tubules elongate using a planar cell polarity-dependent, rosette-based mechanism of convergent extension, *Nature Genetics* **44**, 1382 (2012).

[57] O. Ossipova, K. Kim, and S. Y. Soko, Planar polarization of vangl2 in the vertebrate neural plate is controlled by wnt and myosin ii signaling, *Biology Open* **4**, 722 (2015).

[58] M. Ibrahimi, *Robustness of active anisotropic deformation in developing biological tissues*, Ph.D. thesis, Aix-Marseille Université (2022), 2022AIXM0523.

[59] M. Lefebvre, J. Colen, N. Claussen, F. Brauns, M. Raich, N. Mitchell, M. Fruchart, V. Vitelli, and S. J. Streichan, Learning a conserved mechanism for early neuroectoderm morphogenesis, <https://arxiv.org/abs/2405.18382v1> (2024).

[60] M. Roberts and J. C. Bowman, Dealiasing convolutions for pseudospectral simulations, *Journal of Physics: Conference Series* **318**, 072037 (2011).

[61] J. C. Bowman and M. Roberts, Efficient dealiasing convolutions without padding, *SIAM Journal on Scientific Computing* **33**, 386 (2011), <https://doi.org/10.1137/100787933>.